SANDIA REPORT
SAND2022-13877
Printed October 2022

Sandia National Laboratories

LDRD 226360 Final Project Report: Simulated X-ray Diffraction and Machine Learning for Optimizing Dynamic Experiment Analysis

Tommy Ao, Brendan Donohoe, Marcus Knudson, Carianne Martinez, David Montes de Oca Zapiain, Dane Morgan, Mark Rodriguez, J. Matthew D. Lane

Prepared by
Sandia National Laboratories
Albuquerque, New Mexico 87185
Livermore, California 94550

Issued by Sandia National Laboratories, operated for the United States Department of Energy by National Technology & Engineering Solutions of Sandia, LLC.

Available to DOE and DOE contractors from

U.S. Department of Energy
Office of Scientific and Technical Information
P.O. Box 62
Oak Ridge, TN 37831

Telephone: (865) 576-8401
Facsimile: (865) 576-5728
E-Mail: reports@osti.gov
Online ordering: http://www.osti.gov/scitech

Available to the public from

U.S. Department of Commerce
National Technical Information Service
5301 Shawnee Road
Alexandria, VA 22312

Telephone: (800) 553-6847
Facsimile: (703) 605-6900
E-Mail: orders@ntis.gov
Online order: https://classic.ntis.gov/help/order-methods

LDRD 226360 Final Project Report: Simulated X-ray Diffraction and Machine Learning for Optimizing Dynamic Experiment Analysis

Tommy Ao
Brendan Donohoe
Marcus D. Knudson
Carianne Martinez
David Montes de Oca Zapiain
Mark Rodriguez
J. Matthew D. Lane (PI)
Sandia National Laboratories, Albuquerque, NM 87185 USA

Dane Morgan
Mission Support & Test Services, Los Alamos, NM 87544 USA

SAND2022-13877

ABSTRACT

This report is the final documentation for the one-year LDRD project 226360: Simulated X-ray Diffraction and Machine Learning for Optimizing Dynamic Experiment Analysis.

As Sandia has successfully developed in-house X-ray diffraction tools for study of atomic structure in experiments, it has become increasingly important to develop computational analysis methods to support these experiments. When dynamically compressed lattices and orientations are not known a priori, the identification requires a cumbersome and sometimes intractable search of possible final states. These final states can include phase transition, deformation and mixed/evolving states.

Our work consists of three parts: (1) development of an XRD simulation tool and use of traditional data science methods to match XRD patterns to experiments; (2) development of ML-based models capable of decomposing and identifying the lattice and orientation components of multicomponent experimental diffraction patterns; and (3) conducting experiments which showcase these new analysis tools in the study of phase transition mechanisms. Our target material has been cadmium sulfide, which exhibits complex orientation-dependent phase transformation mechanisms. In our current one-year LDRD, we have begun the analysis of high-quality c-axis CdS diffraction data from DCS and Thor experiments, which had until recently eluded orientation identification.

This work was performed, in part, with Lab Directed Research & Development (LDRD) support.

This manuscript was authored, in part, by Mission Support and Test Services, LLC, under Contract No. DE-NA0003624 with the U.S. Department of Energy and supported by the Site-Directed Research and Development Program, National Nuclear Security Administration, NA-10 USDOE NA Office of Defense Programs (NA-10).

CONTENTS

LIST OF FIGURES

LIST OF TABLES

1. BACKGROUND

1.1. Motivation

X-ray diffraction (XRD) is a powerful diagnostic of atomic structure and is becoming a key tool in studies of the transient states of materials during dynamic compression experiments. Recently, Sandia has successfully demonstrated dynamic XRD capabilities on both the large Z Machine and the small Thor pulser. However, the analysis of XRD patterns of materials undergoing dynamic compression, which are often marred by noise and background, can be highly non-trivial. Thus, a robust simulation and analysis toolkit is needed to optimize interpretation of experimental XRD data.

1.2. Introduction

Dynamic compression experiments have primarily relied upon velocimetry diagnostics, such as Velocity Interferometer System for Any Reflector (VISAR) [2] and Photonic Doppler Velocimetry (PDV) [3], to provide insight into the behavior of materials under extreme conditions at the continuum, macroscopic scale. However, one of the most fundamental properties of a solid is its crystal structure, which requires atomic, microscopic scale understanding. X-ray diffraction is a key atomic scale probe since it provides quantitative observation of the compression and strain of the crystal lattice, and is used to detect, identify, and quantify phase transitions. While XRD measurements under static pressures are routinely performed on single and polycrystalline samples, similar measurements on dynamic compression experiments are more challenging. X-ray diffraction data from dynamically compressed samples are extremely valuable as direct measurement of the elastic compression of the crystal lattice, onset of plastic flow, strength-strain rate dependence, phase transitions, and density of crystal defects such as dislocations.

In-situ dynamic XRD has been performed at gas gun [4] and laser-driven [5, 6] dynamic compression facilities in various forms, including monochromatic Bragg reflection [7] and transmission [8, 9], multi-line Laue pattern [10], and time-resolved measurements [11, 12, 13]. However, implementing XRD on pulsed-power platforms has been challenging due to their unique experimental issues, such as load hardware constraints, high X-ray background, electromagnetic pulse interference, and debris mitigation. After overcoming all of those challenges, XRD has recently been successfully implemented on Sandia's Z Machine [14, 15] and Thor pulser [16, 17].

Experimental diffraction patterns from simple structures can often be readily identified through comparison with databases or idealized structure calculations. However, when dynamically compressed lattices and orientations are not known, *a priori*, identification can become an

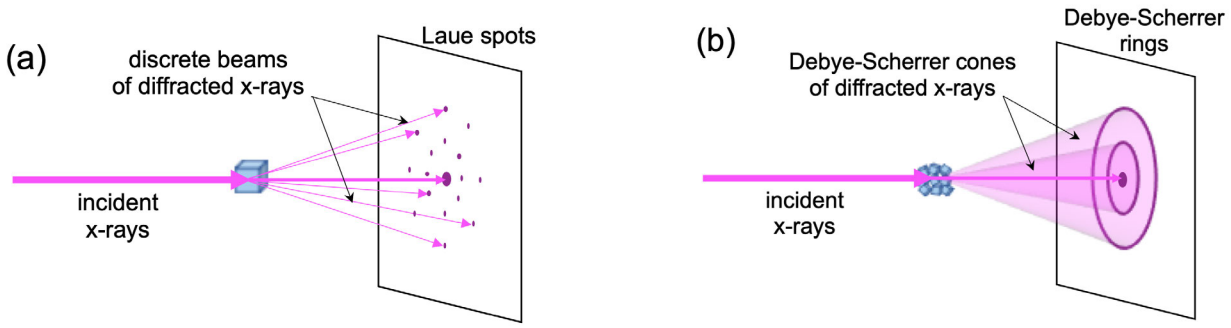

Figure 1-1. Monocrystalline vs. polycrystalline XRD. (a) In a monocrystalline material, the individual reciprocal lattice points are projected onto the detector as discrete peaks. (b) In polycrystalline material with randomly oriented crystals the reciprocal lattice points for each of the crystallites combine to form Debye-Scherrer cones.

exhausting search of possible final states. For highly deformed lattices, or when multiple lattices or orientations are convolved, this method quickly becomes untenable. We propose incorporating machine learning (ML) convolutional neural network approaches that will enable pattern recognition from the near-limitless permutations – selecting high-probability matches to experimental data from large datasets of simulated patterns.

A new 2D XRD pattern simulation capability has been added to the Large-scale Atomic/Molecular Massively Parallel Simulator (LAMMPS) code [18] to calculate diffraction images from arbitrary atomic systems, including from all lattice symmetries, mixed states, powders, and microstructural defects. This work will enable enhanced pattern recognition of both single crystal and powder diffraction patterns. Machine learning algorithms will leverage the simulated diffraction data to empower analysis of experimental patterns obtained from Z and Thor. Success will dramatically improve atomic- scale understanding and predictive capability of phase transition behavior.

1.3. XRD Theory

Crystalline solid materials consist of atoms arranged in a definite, repeating pattern in three dimensions, called a Bravais (crystal) lattice [19]. In 3D space, there are 14 Bravais lattices that are grouped into 7 lattice systems: triclinic, monoclinic, orthorhombic, tetragonal, cubic, trigonal, and hexagonal. For example, there are 3 lattices in the cubic system: the simple cubic (sc) lattice, the body-centered cubic (bcc) lattice, and face-centered cubic (fcc) lattice. The structure of a crystalline material may be represented geometrically by Hermann–Mauguin notation, which defines its symmetries in terms of point, plane, and space groups. A point group is a group of geometric symmetries that keep at least one point fixed. The symmetry elements that constitute the point groups are proper rotation axes (n), mirror planes (m), inversion center ($\bar{1}$), and rotary inversion axes ($\bar{n}$). A plane group is a mathematical classification of a 2-dimensional repetitive pattern, whose first letter is either lowercase p or c to represent primitive or centered unit cells. The next number is the rotational symmetry, and the presence of mirror planes are denoted by m and glide reflections are denoted by g.

A space group is the symmetry group of a configuration in 3-dimensional space. The symbol of a space group is defined by combining the uppercase letter describing the lattice type with symbols specifying the symmetry elements. The Bravais lattice types are P = primitive, I = body centered (German "Innenzentriert"), F = face centered (German "Flächenzentriert"), A = base centered on A faces only, B = base centered on B faces only, C = base centered on C faces only, and R = rhombohedral. For example, the mineral form of sodium chloride (NaCl) is commonly known as rock salt, which has the space group notation of $Fm\bar{3}m$ in Hermann-Mauguin notation. The reciprocal lattice represents the Fourier transform of the Bravais lattice that exists in real (physical) space and exists in reciprocal or momentum space (k-space). Crystallographic planes are described using Miller indices (hkl), which are the integer coefficients of the reciprocal lattice vectors. In the process of XRD, the momentum difference between incident and diffracted X-rays of a crystal is a reciprocal lattice vector. The XRD pattern of a crystal can be used to determine the reciprocal vectors of the lattice, thus reconstructing the atomic arrangement of the crystal. Figure 1-1 presents the XRD patterns measured by a 2D X-ray detector of ideal monocrystalline and polycrystalline materials.

A monocrystalline material or single-crystal has an atomic structure that repeats periodically across its whole volume, where each atom is related to every other equivalent atom in the structure by translational symmetry. The entire monocrystalline sample is continuous and unbroken to the edges of the sample, with no grain boundaries. For an ideal monocrystalline material, the individual reciprocal lattice points are projected onto the detector as discrete peaks called Laue spots at associated diffraction angles. The locations of the measured peaks are used to determine the values of the (hkl) planes that from which the X-rays were diffracted from (see Figure 1-1(a)).

A polycrystalline material, or polycrystal, is made up of an aggregate of many small crystallites, or grains, each having a high degree of order. These grains vary in size and orientation with respect to one another. In metals, grain interfaces or boundaries are very important in determining their properties. When a polycrystalline sample is illuminated by a monochromatic X-ray beam, each orientation reflects X-rays to a different location on a Debye-Scherrer cone [20, 21]. The Debye-Scherrer cone is the superset of the reflections formed by the crystal that satisfy Bragg's Law. For a powder where nearly all orientations are represented, the reflections combine to form uniform cones of diffracted X-rays onto an X-ray detector called Debye-Scherrer rings (see Figure 1-1(b)) Unlike powders, polycrystals do not consist of randomly oriented crystallites. Rather, metal polycrystalline samples have grains of varying sizes and preferential orientations (texture), which tend to produce incomplete or spotty diffraction rings on the X-ray detector.

2. EXPERIMENTS

2.1. Methodology

Dynamic compression techniques have been used extensively to collect information on the high-pressure equation of state (EOS) of materials. Most high-pressure EOS data have been obtained from shock compression which represents to determine the response of a material along its principal Hugoniot; i.e., the states produced by the passage of a steady, single shock wave produced from ambient conditions or by shock compression of porous samples of the material, which produce higher temperature states at a given compression [22, 23, 24]. The thermodynamic states produced by ramp loading of all materials, and solids in particular, are closer to the isentrope because entropy and heat producing shock fronts are avoided [25, 26, 27, 28, 29].

To perform dynamic XRD experiments, various dynamic compression drivers have been coupled to X-ray sources. Specifically, small gas gun and laser drivers have been built at large X-ray source facilities, such as the Dynamic Compression Sector (DCS) at the Advanced Photon Source (APS) [4] and the Matter in Extreme Conditions (MEC) hutch at the Linac Coherent Light Source (LCLS) [6]. However, pulsed-power platforms are much harder to construct at these X-ray source facilities because of their large size and unique mode of operation.

To generate X-rays for XRD on Z, the multi-kJ Z-Beamlet laser (ZBL) is focused onto a metal foil target, forming a high temperature plasma that emits K-shell line radiation. These He-like emissions, specifically He_α lines, of various metals with a range of X-ray photon energies (4–10 keV) are used to probe the dynamically-compressed material states generated on Z-Dynamic Material Properties (DMP) loads. Alternatively, a compact, pulsed-power X-ray source has been implemented on Thor to enable XRD measurements. This compact flash X-ray diode can generate a single, bright ($\sim$30 ns) pulse of narrow line emission (e.g., Mo–K_α, 17.4 keV, 0.71 Å) [30, 31] for use on Thor-XRD experiments, along with the broadband bremsstrahlung emission of up to 300 keV.

2.2. Ambient Results and Discussion

To produce ambient XRD data for the LAMMPS-ML testing, the Thor-XRD setup was replicated on a benchtop, as shown in see Figure 2-1. The X-ray diode head was mounted so the X-rays are horizontal to the lab bench. The XRD sample and the image plate (IP) X-ray detector were mounted onto a multi-axis stage with a total of 5° of motion: x-, y-, and z-translations, and pitch- and yaw-rotations (see Figure 2-1(a)). In addition, the XRD sample was placed on an independent yaw-rotation stage, and the IP was mounted to an independent x-y-stage. A direct beam block

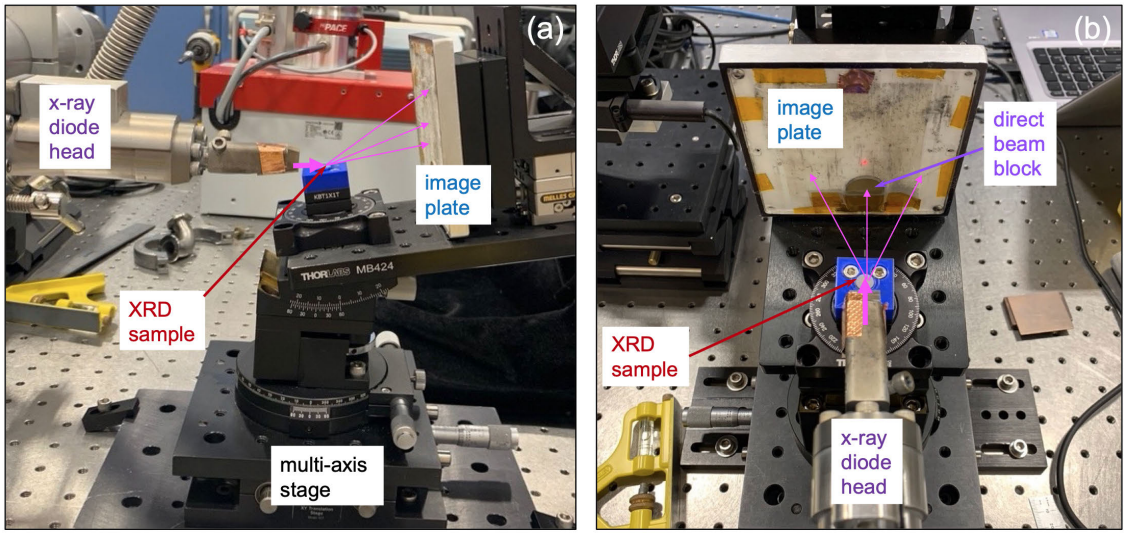

Figure 2-1. Photos of setup for benchtop ambient XRD testing with (a) side and (b) top views.

made of W-Cu was placed on the IP to attenuate the strong 0° X-ray direct beams, as shown in Figure 2-1(b).

Cadmium sulfide (CdS) is a yellow solid that at ambient conditions (density of 4.83 g/cm^3) occurs in two crystal forms: (1) the more stable wurtzite-hexagonal structure ($P6_3mc$), and (2) the less common zincblende-cubic structure ($F\bar{4}3m$). Single-crystal CdS samples (wurtzite structure) with two different orientations, c-axis and a-axis, were obtained from the vendor SurfaceNet GmbH. The c-axis CdS sample has the (0001) axis perpendicular its flat surfaces, while the a-axis CdS sample has the (11-20) axis perpendicular to its flat surfaces.

Using the Thor-XRD benchtop setup, a series (0-180° rotation at 10° increments) of ambient XRD patterns were obtained from an a-axis CdS (8 mm diameter, 1mm thick) sample, as shown in Figure 2-2. With the XRD sample rotation stage was at 0°, the edge of the CdS sample was marked to provide an angular reference point, denoted as the "DICE mark" (see Figure 2-2(a)). A thick Mo anode (3mm diameter) was installed in the X-ray diode head so all of the shots could be completed without needing to change the anode. The incident X-rays were at 11° relative to the CdS sample's surface. The IP detector was located at 65 mm from the center of the CdS sample. The direct X-ray beam was attenuated with a W-Cu block.

A total of 19 Thor-XRD shots (0-180° rotation at 10° increments) were performed to obtain the XRD data set. The measured IP data of the XRD patterns are shown in Figure 2-3 to Figure 2-9. The direct beam along with the shadow of the W-Cu beam block were observed at the center top of each XRD pattern. Various XRD Laue spots from the CdS sample were observed within the lower 2/3 of the IP data. As the CdS sample was rotated, some Laue spots disappeared while new ones appeared. After examining the complete a-axis CdS sample XRD data set, the c-axis, which is parallel to the crystal face, was predicted to occur with the DICE mark at 55°. To validate the prediction, two more Thor-XRD shots were performed with (1) the DICE mark at 55° so the X-rays would be parallel to the c-axis (see Figure 2-2(b)), and (2) DICE mark at 145° so the X-rays would be perpendicular to the c-axis see Figure 2-2(c)). The prediction was indeed

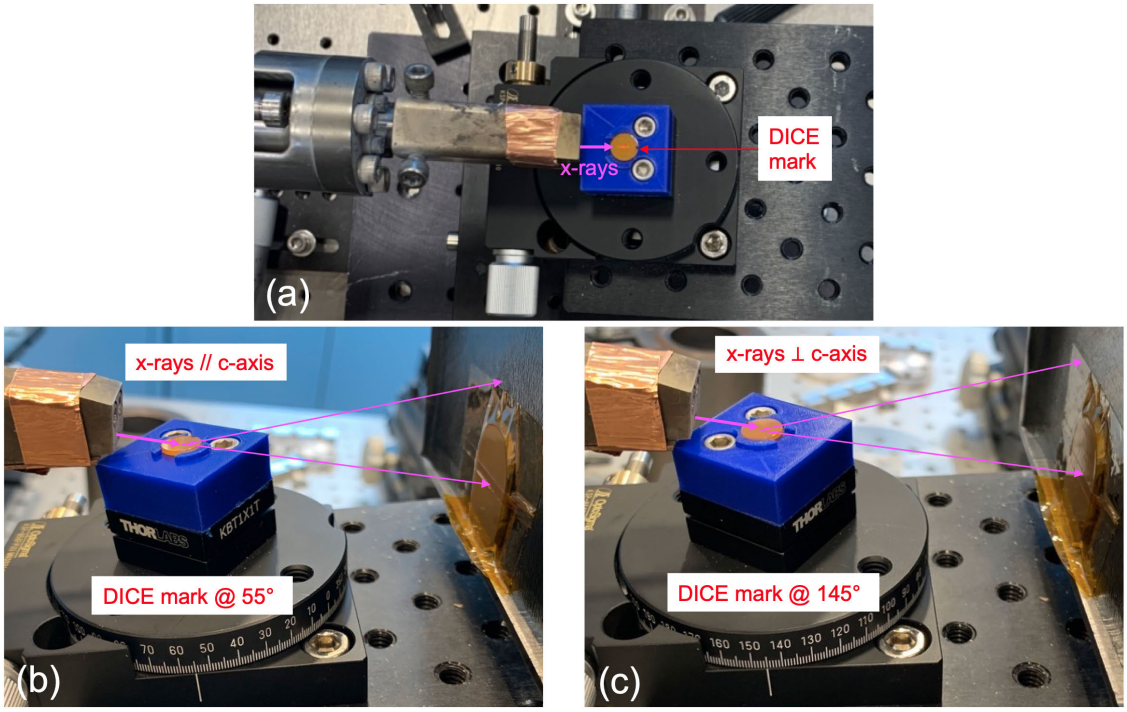

Figure 2-2. Photos of CdS (a-axis) 180 ° rotation setup (a) top view, (b) X-rays parallel to c-axis, and (c) X-rays perpendicular to c-axis.

confirmed based on the symmetry of the observed Laue spots shown in Figure 2-5(a)) and Figure 2-8(b).

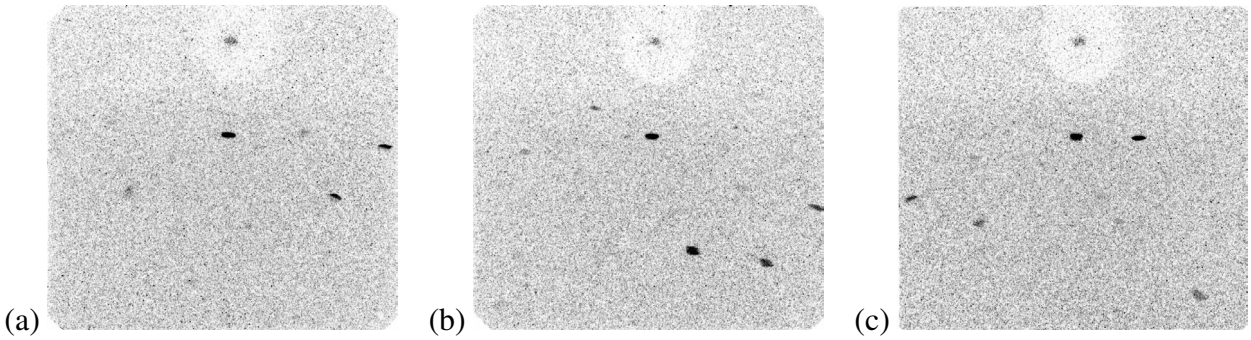

Figure 2-3. IP data of CdS (a-axis) with DICE mark at (a) 0°, (b) 10°, and (c) 20°.

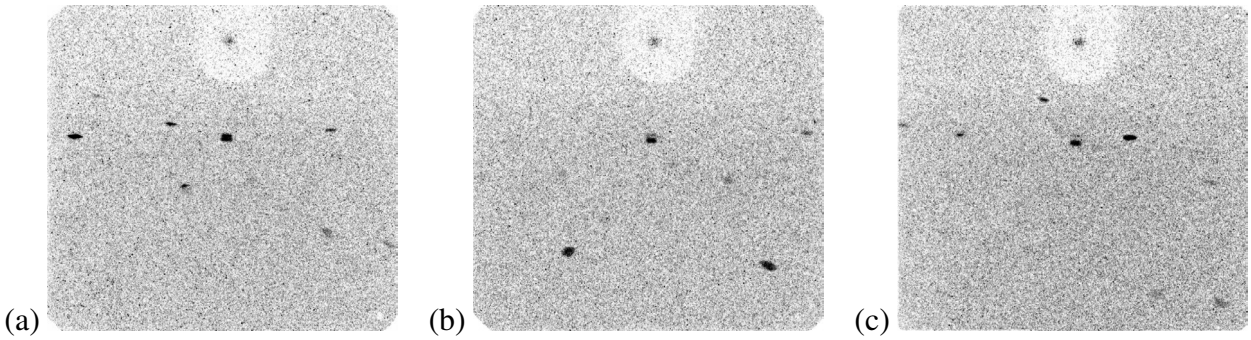

Figure 2-4. IP data of CdS (a-axis) with DICE mark at (a) 30°, (b) 40°, and (c) 50°.

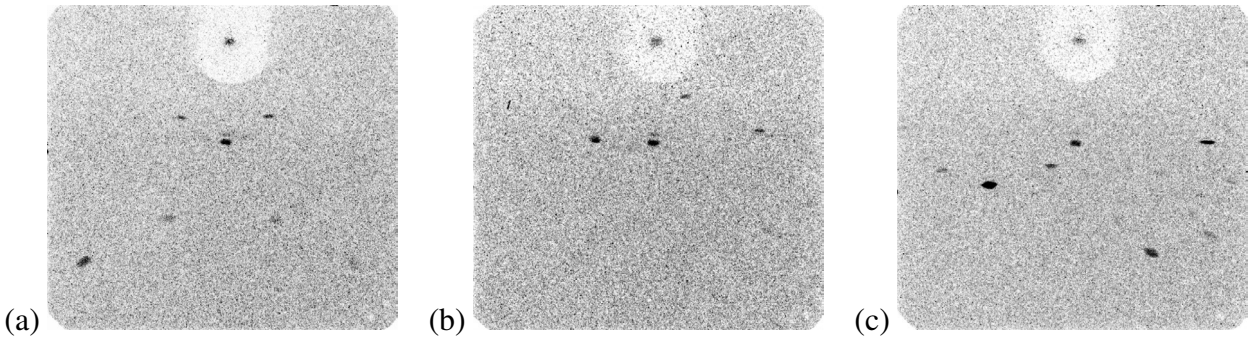

Figure 2-5. IP data of CdS (a-axis) with DICE mark at (a) 55°, (b) 60°, and (c) 70°.

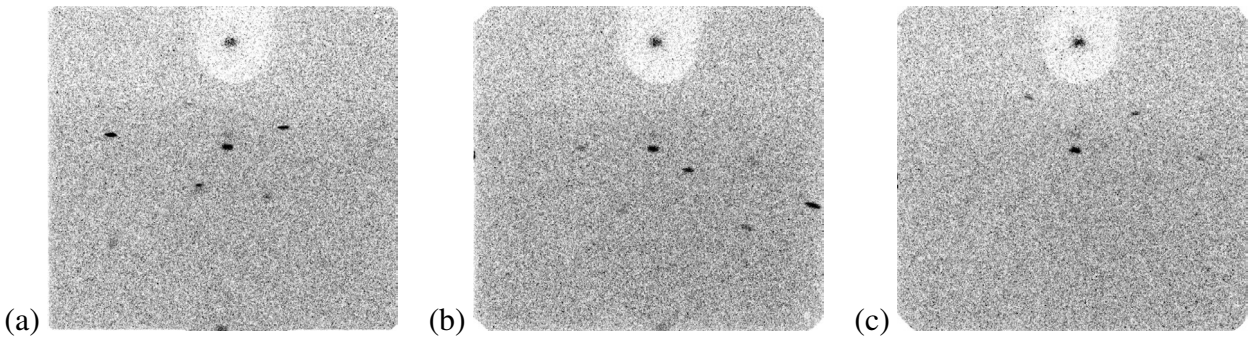

Figure 2-6. IP data of CdS (a-axis) with DICE mark at (a) 80°, (b) 90°, and (c) 100°.

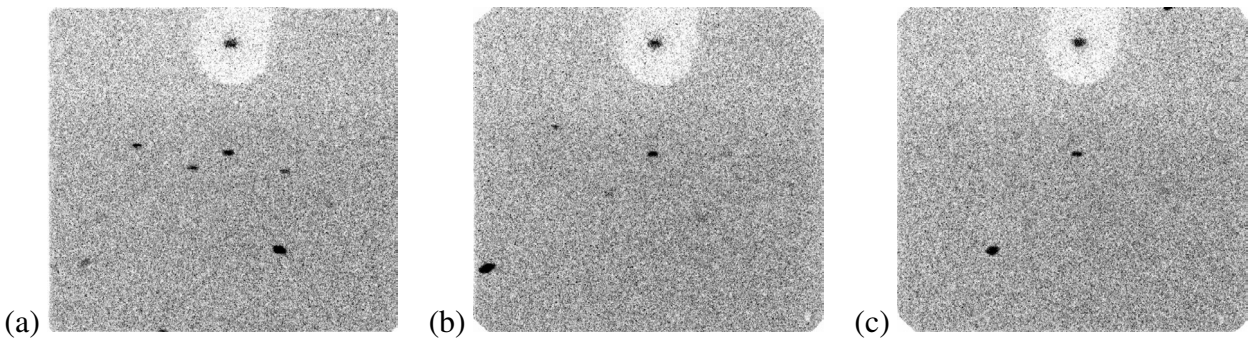

Figure 2-7. IP data of CdS (a-axis) with DICE mark at (a) 110°, (b) 120°, and (c) 130°.

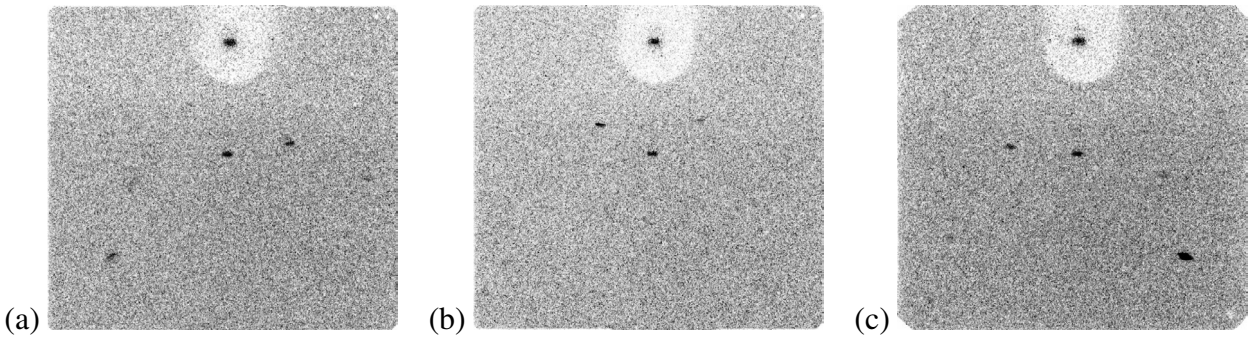

Figure 2-8. IP data of CdS (a-axis) with DICE mark at (a) 140°, (b) 145°, and (c) 150°.

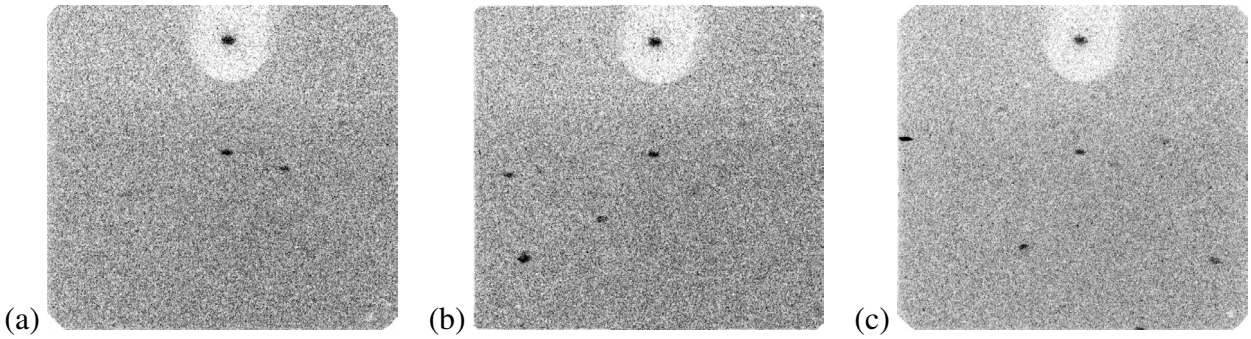

Figure 2-9. IP data of CdS (a-axis) with DICE mark at (a) 160°, (b) 170°, and (c) 180°.

2.3. Dynamic Results and Discussion

In solid-solid phase transitions the lattice mismatch at the interface between the two phases will add to the energy barrier for the transition [32]. The magnitude of this additional energy barrier likely depends upon the deformation state of the parent phase. This raises some very fundamental questions: Is a shock-induced transformation influenced by the deformation state (i.e., elastic versus inelastic) of the parent phase? Can the transformation mechanism in a single crystal depend upon the direction of shock propagation? What is the role of inelastic deformation in the transformation kinetics? Here we examine the role of inelastic deformation in shock-induced phase transformations with in-situ, time-resolved X-ray diffraction measurements in single-event, shock wave experiments on cadmium sulfide (CdS) single crystals.

Despite the considerable body of work on shock-induced phase transformations, very little is known regarding the role of inelastic deformation in both the transformation mechanism and kinetics. CdS, which exhibits a stress-induced phase transition from the ambient wurtzite (hcp) structure to the high-pressure rock salt (fcc) structure at ~3 GPa [33, 34, 35, 36, 37], is an ideal system to address the role of deformation and crystal orientation. CdS exhibits dramatic differences in its elastic-inelastic behavior for shock compression along the crystal a- and c-axes: shock propagation along the c-axis does not exhibit inelastic deformation prior to the phase transition [33], while shock propagation along the a-axis exhibits inelastic deformation at ~2.5 GPa [34], well below the phase transition threshold. These differences enable evaluation of the phase transition mechanism and kinetics for the same system under significantly different

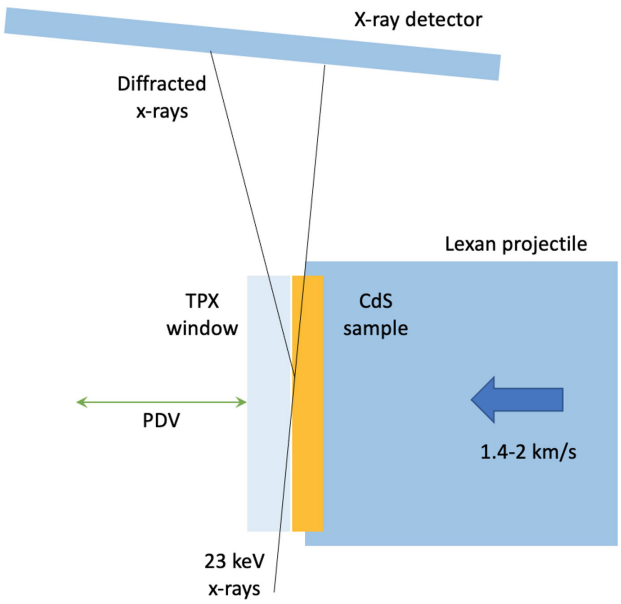

Figure 2-10. Experimental configuration for in-situ, time-resolved X-ray diffraction measurements in single-event, shock wave experiments on CdS single crystals.

deformation states.

Furthermore, previous optical spectroscopy [35, 36, 37] studies on CdS show a dramatic reduction in transformation timescale for compression above ∼5 GPa along the c-axis. We propose this is due to the onset of inelastic deformation at ∼5 GPa, well above the phase transition threshold. This hypothesis, based solely on the previous studies, is speculative; X-ray diffraction measurements can definitively address this issue. Finally, the transformation in CdS appears to progress through an intermediate or metastable crystal structure [33, 34, 35, 36, 37, 1]. However, direct observation of a metastable structure in a shock-induced phase transformation has not been reported; X-ray diffraction (XRD) measurements could provide such an observation.

XRD experiments on shocked single crystal CdS were performed using the powder gun in the 35-ID-E station at the Dynamic Compression Sector (DCS) at the Advanced Photon Source (APS) at Argonne National Laboratory. The experimental configuration used, referred to as a front surface impact configuration, is illustrated in Fig. 2-10. A 750 μm thick, 10 mm diameter CdS single crystal sample (SurfaceNet, GmbH) was mounted on a lexan projectile and impacted a 1.4 mm thick polymethylpentene, commonly referred to by its trade name TPX (Mitsui Chemicals, Inc.), window; thick enough to provide a high-stress state in the CdS for ∼500 ns, the time duration of interest in these experiments.

XRD data was obtained in the reflection geometry using the first harmonic of the U17.2 undulator (which produced a ∼23.5 keV pink X-ray beam) with a 5° incident angle between the X-rays and the shock propagation axis. Given the absorption depth of CdS at 23.5 keV (∼200 μm) and the shallow incident angle, this configuration preferentially probed the sample near the impact surface (∼20 μm depth). During the impact event, two or three XRD patterns were obtained from ∼100 ps synchrotron X-ray pulses with separation of ∼153 ns between pulses (24 bunch mode at the APS). At each stress level of interest, multiple experiments were performed to randomly sample

the crystal within the first ∼300 ns after impact (dictated by the 153 ns X-ray time structure). Because the configuration preferentially probes the sample near the impact surface, these snapshots provided XRD data at various times after the shock entered the sample, thereby providing time resolved data.

XRD signals were recorded using a framing X-ray area detector, comprised of a 150 mm phosphor screen optically coupled to image intensified CCD cameras. The phosphor screen, which was located ∼120 mm from the TPX window and oriented perpendicular to the X-ray beam, converted the X-ray photons to optical photons. Optical photons were coupled via lenses and beam splitters to 4 separate image intensified CCD cameras triggered at 153 ns intervals to capture images from subsequent X-ray bunches produced by the synchrotron. Experimental timing was structured such that the first frame was obtained just prior to impact of the CdS sample with the TPX window; subsequent frames were obtained after impact. In addition to XRD measurements, velocity interferometry data (Photonic Doppler Velocimetry, PDV) were obtained from the impact surface (CdS/TPX interface) during each experiment. These data provided a measure of the stress at the impact surface as a function of time, enabling correlation of the XRD measurement(s) with the stress state at the impact surface; the region being preferentially probed in reflection geometry.

Based on the results of previous front surface impact experiments [1], initial experiments at DCS were performed on c-axis CdS at three different elastic impact stresses (the stress achieved at the impact surface assuming purely elastic response of the ambient wurtzite phase); approximately 3.9, 4.8, and 5.4 GPa. These stress levels also correspond to those achieved in front surface impact velocimetry experiments performed by Jones and Gupta [1], which provide a time resolved measure of the stress at the impact surface, as seen in Fig. 2-11. At the two lower stresses, the initial response appears to be elastic compression (first ∼100 and ∼20 ns at 3.9 and 4.8 GPa, respectively) followed by transformation to an intermediate structure (subsequent ∼100 ns) followed by transformation to the final rock salt structure. At the highest stress, the elastic impact stress is not resolved; it is speculated that transformation to an intermediate structure occurs on a sub-ns timescale, followed by transformation to the final rock salt structure over ∼200 ns. These transitions occur on timescales that are compatible with the X-ray time structure of the APS.

Initial experiments at DCS have demonstrated that high-quality XRD data can be obtained from shocked CdS single crystals. Representative data from experiment 19-4-060, in this case an elastic impact stress of 3.7 GPa, is shown in Fig. 2-12. The first image (Fig. 2-12a) was obtained ∼78 ns prior to impact and represents diffraction from the ambient wurtzite structure. These data enable the orientation of the crystal with respect to the X-ray beam and shock propagation axis to be determined. In this case the crystal a-axis was established to be ∼-3.6 ° off the vertical axis (the axis perpendicular to both the X-ray beam and the shock propagation axis). The second frame (Fig. 2-12b) was obtained ∼75 ns after impact. The locations of the diffraction spots are similar to those observed in the first frame and are consistent with what would be expected from elastically compressed wurtzite, exhibiting slight elongation in the radial direction. The third frame (Fig. 2-12c) was obtained ∼228 ns after impact and looks markedly different, indicative of a significant change in the crystal structure suggesting that a phase transformation has occurred. The highly localized diffraction spots also suggest that the high-pressure phase retains a very high

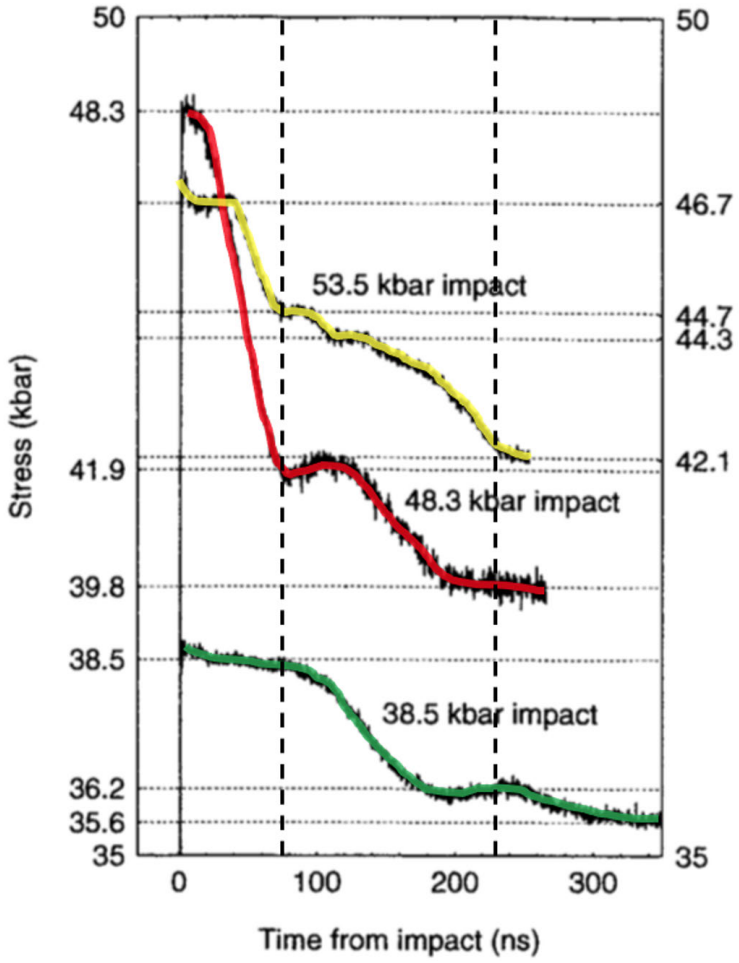

Figure 2-11. Velocimetry data from front surface impact experiments described in Ref. [1]. The dashed vertical lines correspond to times at which XRD images were obtained in experiment 19-4-060, shown in Fig. 2-2. This figure adapted from Ref. [1].

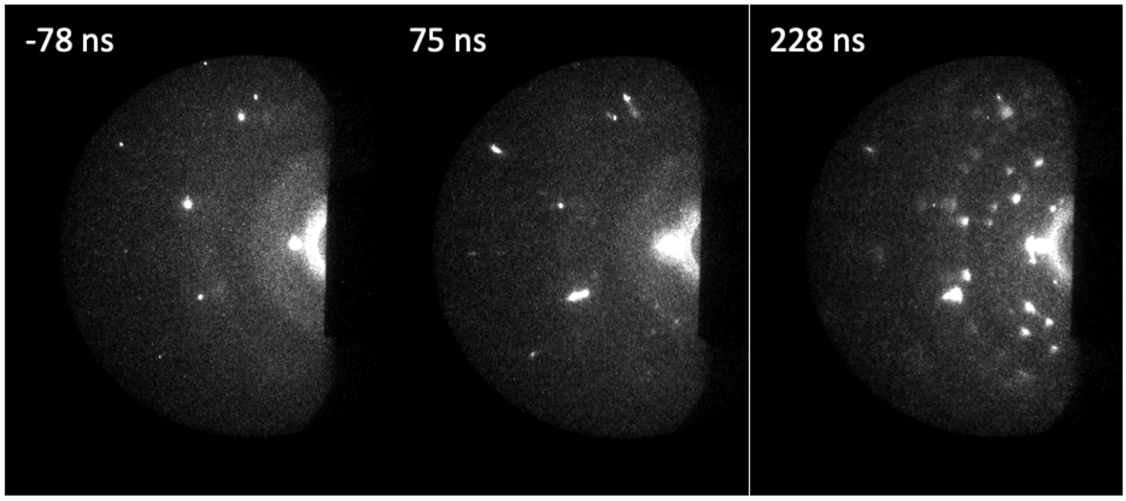

Figure 2-12. Representative XRD patterns from experiment 19-4-060, in this case an elastic impact stress of 3.7 GPa. Leftmost frame was obtained prior to impact and corresponds to diffraction from the ambient wurtzite phase. The middle frame was obtained 75 ns after impact and corresponds to elastically compressed wurtzite. The rightmost frame was obtained 228 ns after impact and clearly exhibits new diffraction spots indicating a significant change in the crystal structure suggesting that a phase transformation has occurred.

degree of texture, indicating that there is a strong orientation relation between the daughter and parent phases.

The relatively broad spectrum of the pink beam at DCS, shown in Fig. 2-13, complicates the analysis of the XRD patterns for single crystal samples. For a given observed diffraction spot it is not known a priori what X-ray energy satisfied the Bragg condition to produce that spot; it is only known that the energy lies within the spectrum shown in Fig. 2-13. Thus, the following procedure was followed to index the ambient CdS crystal orientation from the pre-impact XRD pattern. First, multiple (at minimum three, but preferably more) reasonably strong diffraction spots were selected from the XRD image. Geometrical considerations were then used to determine the scattering angles and all *hkl* indices possible for each diffraction spot based on the minimum and maximum X-ray energy and the nominal initial crystal orientation (i.e., c-axis aligned along the direction of shock propagation). All possible *hkl* combinations are then evaluated to determine how well the set of angles between candidate *hkl* vectors match the inferred angles from the measured diffraction spots. This routine typically identifies a set of reciprocal lattice vectors that best match the measured XRD pattern. These reciprocal lattice vectors are then randomly varied by small angular rotations until the root mean square difference between the calculated and measured diffraction spots satisfy a minimum difference criterion. This method is reasonably robust, provided that the selected diffraction spots originate from unique crystal lattice planes.

Similarly, the broad spectrum of the pink beam complicates analysis of the XRD patterns obtained from the phase transformed material. While a direction normal to the corresponding lattice plane of the phase transformed structure can be calculated from each localized diffraction spot, this is not sufficient to specify the orientation relation between the ambient and phase transformed structures. In particular, because of the degeneracy of the phase transformed structure, it is not possible to deduce that two observed diffraction spots from different lattice

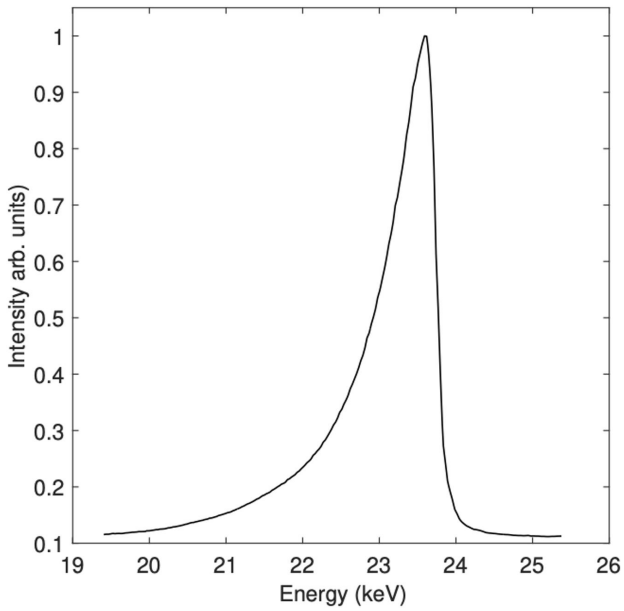

Figure 2-13. Measured spectral flux of the pink beam at DCS; in this case the first harmonic of the U17.2 undulator.

planes correspond to a single orientation. In practice, forward simulations – including all possible degeneracies – are required to determine whether the measured XRD patterns are consistent with a proposed phase transition mechanism. Such a process requires a cumbersome and sometimes intractable search of possible final states. This problem is exacerbated and becomes untenable when lattices are highly deformed, and especially when multiple lattices or orientations are convolved. For this reason, we have proposed incorporating machine learning (ML) using convolutional neural network approaches to enable pattern recognition from the near-limitless permutations – selecting high-probability matches to experimental data from large sets of simulated data, as discussed in Chapter 3.

3. LAMMPS SIMULATIONS

3.1. Producing LAMMPS X-ray Diffraction Simulations

In this one-year LDRD we established Sandia's in-house capability to produce simulated 2D diffraction pattern data from arbitrary atomistic structures. We did this by extending the USER-DIFFRACTION package in the LAMMPS molecular dynamics code [18] to allow the calculation of 2D X-ray diffraction patterns. Working with the original package developer, Shawn Coleman (currently at Army DEVCOM), we have demonstrated and validated our capability. Significant further work will be needed to improve its generalizability, efficiency and useability. However, the tool is already able to handle the polychromatic, uncollimated X-ray sources used in Thor experiments, and has been used to identify unexpected mechanisms in experiments conducted by Knudson, et al. at the Dynamic Compression Sector.

3.1.1. Method of Reciprocal Lattice Calculation

Diffracted X-rays are produced when a collimated X-ray beam interacts and coherently scatters via the electrons present in the atomic lattice planes within crystalline structures. The diffraction pattern is given by the condition for positive interference and by the crystal's interplanar separation. The Bragg diffraction condition is

$$\frac{\sin(\theta)}{\lambda} = \frac{|\,\vec{k}\,|}{2} \tag{3.1}$$

where θ is the diffraction angle, λ is the X-ray wavelength, and $\vec{k}$ is the vector difference between the wave vectors of the incident X-ray and the lattice planes, $\vec{k} = \vec{k}_D - \vec{k}_I$. The X-ray diffraction intensity, $I_x(\vec{k})$, from [14], for a collection of atoms can be written as a function of the structure factor of the collection of atoms,

$$I_x(\vec{k}) = Lp(\theta)\frac{F(\vec{k})F^*(\vec{k})}{N} \tag{3.2}$$

where the structure factor, $F(\vec{k})$, is calculated from a sum over all atoms as follows,

$$F(\vec{k}) = \sum_{j=1}^{N} f_j(\theta)\exp(2\pi i\,\vec{k}\cdot\vec{r}_j) \tag{3.3}$$

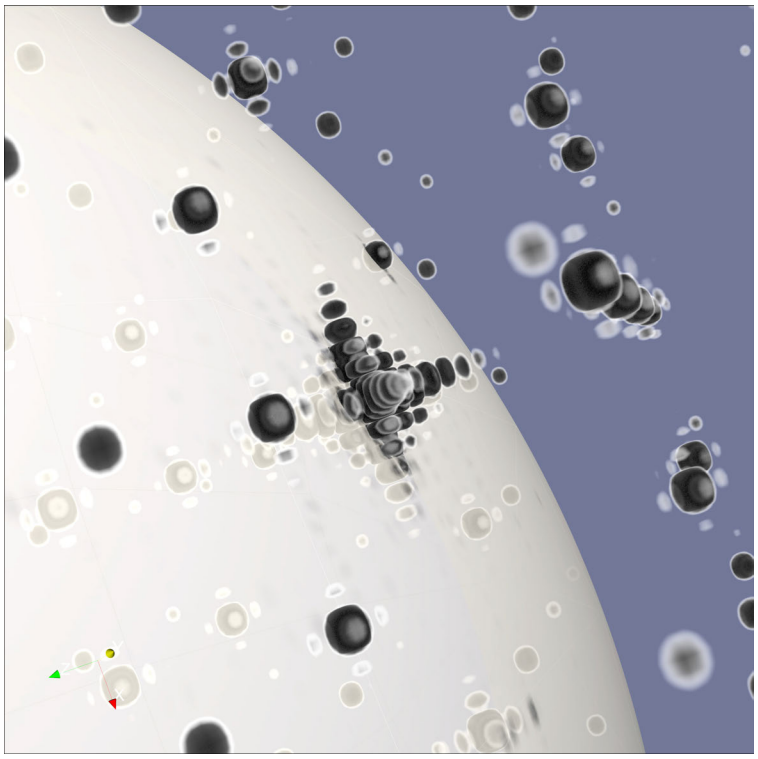

Figure 3-1. Representation of a reciprocal lattice density (black) and Ewald sphere construction (white) in k-space. The points intersecting the Ewald sphere of radius $1/\lambda$ represents the monochromatic diffraction pattern for that energy X-ray. The orientation of the sphere is determined by the incident k vector. The 2D diffraction pattern in mapped on the spherical surface with angular coordinates θ and ϕ.

where the f_j are the atomic scattering factors and $\vec{r}_j$ represent the atomic positions. The Lorentz-polarization factor, $Lp(\theta)$, is given by,

$$Lp(\theta) = \frac{1+\cos^2(2\theta)}{\cos(\theta)\sin^2(\theta)} \tag{3.4}$$

The 2D diffraction pattern can be determined by a geometrical construction (see Fig. 3-1) in which the diffraction pattern is given by the intersection of the Ewald sphere of radius $1/\lambda$ with the reciprocal space diffraction intensity, $I_x(\vec{k})$.

3.1.2. LAMMPS Scripting and Output

A sample script is given below for producing a reciprocal representation of the structure CdS_190527_003_180.data which is a relatively small (65000 atom) system. Typical systems should contain at least 500,000 atoms. This script produces a vtk file with a high resolution (0.005 $Å^{-}1$).

```
#SCRIPT:  CdS_xrd.in to create CdS_001.xrd.0.vtk
  4 units           metal
  5
  6 atom_style      charge
  7 boundary        p p p
  8
  9 read_data       CdS_190527_003_180.data
 10 replicate       2 2 2
 11
 12 # Define atom properties
 13 mass            1 112.41
 14 mass            2 32.065
 15
 16 group Cd type 1
 17 group S type 2
 18
 19 set group Cd charge  1.18
 20 set group S charge -1.18
 21
 22 # Define force field
 23
 24 timestep 0.001
 25
 26 pair_style      lj/cut/coul/cut 10.0
 27 pair_modify     shift yes mix arithmetic tail no
 28
 29 pair_coeff      1 1  1.447711e-3 1.98 10.0
 30 pair_coeff      2 2  1.421859e-3 4.90 10.0
 31
 32 dump    d1 all custom 1000 CdS.dump id type x y z ix iy iz vx vy vz
 33
 34 thermo_style custom step temp pe etotal pxx pyy pzz lx ly lz vol
 35 thermo          100
 36
 37 atom_modify     sort 0 0
 38
 39 compute  XRD all xrd  0.7107 Cd S 2Theta 1 179 c 0.005 0.005 0.005 manual LP 1 echo
 40 fix      2 all xrd/vtk 1 1 1 c_XRD file $A_001.xrd
 41
 42 dump            1 all custom 1000 $A.dump id x y z
 43 run             0
```

3.2. From Monochromatic Calculations to Realistic Experimental Comparisons

The procedure described in Section 3.1 is sufficient to produce a very idealized 2D diffraction pattern for an arbitrary collection of atoms. However, initial comparisons with experiments were quite poor. We quickly determined that the experimental image plates we produced were far from ideal in ways that had significant impact on our comparisons. Ultimately, we determined that four realistic aspects of the experiments would need to be modeled explicitly in order to reproduce the experimental patterns.

To compare well with experimental diffraction patterns, we needed to extend the LAMMPS simulations to account for:

- Broad energy spectrum (i.e. polychromatic) source X-rays.
- Uncollimated X-ray sources.
- Projection distortion on the image plate (flat/spherical, and keystoning due to tilt).
- Precise geometry/orientation beyond typical measurement uncertainty.

The first three of these aspects will be described in this section, the last will be discussed in the section on applications.

3.2.1. Source-appropriate Polychromatic X-ray Spectrum

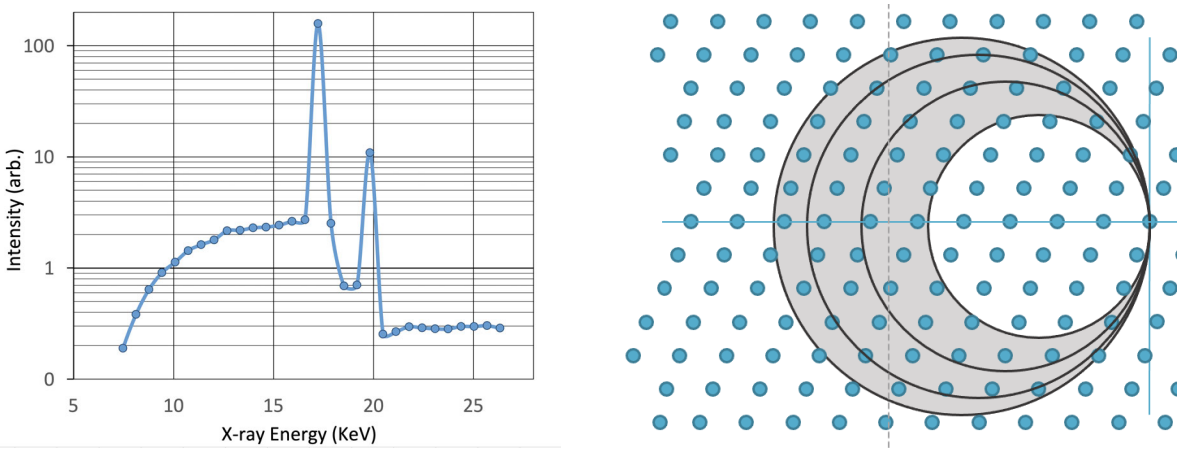

Figure 3-2. The monochromatic Ewald sphere construction can be generalized for multiple X-ray energies. A continuous energy spectrum can be approximated with a superposition of discrete spheres. Left: the energy spectrum of the molybdenum X-ray diode emission. This source when filtered is often approximated as monochromatic, but in fact the bright K_α and K_β lines have a broad effective spectrum of bremsstrahlung radiation. Right: a depiction in two dimensions of the areal intersection of the Ewald circle with a reciprocal lattice. Each discrete circle (sphere in 3D) is scaled by the appropriate X-ray intensity. Every source has a unique spectrum.

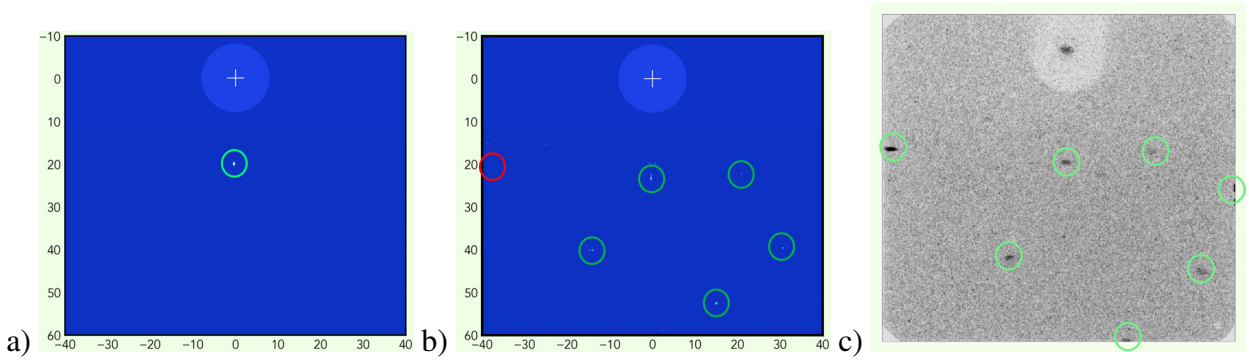

Figure 3-3. Calculated and experimental diffraction patterns. (a) Simulated diffraction pattern produced with a monochromatic X-ray source (i.e. single Ewald sphere radius) at the K_α wavelength. (b) Simulated polychromatic diffraction pattern produced by numerical integration of the discrete points of the Mo X-ray diode spectrum shown in Fig. 3-2. (c) The corresponding experimental diffraction pattern (180° from DICE mark) as seen in Fig. 2-9

At the start of the year, we had believed that we might be able to model the experimental diffraction patterns from Molybdenum X-ray diodes with monochromatic X-rays matched to the dominant K_α line of the emission. This seemed reasonable because this line is at least 10x brighter than the bremsstrahlung background, as seen in Figure 3-2 (Left). As it turned out, we not only required the secondary K_β peak but quickly discovered that the full polychromatic spectrum calculation would be required. To our advantage, the Ewald sphere method for monochromatic diffraction determination was easily generalized by repetition with spheres of various radii - each radius given by a different X-ray wavelength. In this way, the known X-ray spectrum of a source could be discretized and the the monochromatic 2D diffraction pattern determined. The polychromatic pattern was then constructed by superposition of these components, each scaled appropriately by the respective source intensity depicted (for molybdenum) in Fig. 3-2. Each polychromatic pattern requires the contribution of many monochromatic calculations. We found 20 to 40 contributions in this numerical integration to be sufficient to approximate the experiments.

We see from Figure 3-3 that our simulations do much better at capturing the shape and size of the experimental image plate scans when we properly account for the broadening due to the pin hole geometry.

3.2.2. Uncollimated Source Broadening

The calculation from LAMMPS assumes that the incident beam is a plane wave without any angular spread. This approximation can be quite good for nearly collimated X-ray sources, such as a the Advanced Photo Source (APS) at Argonne National Lab. However, our X-ray diode source on Thor is currently quite simple by comparison – an effective point source with a pin-hole filter. In this arrangement, generally, small pin holes which are relatively far from the source produce nearly collimated X-rays, but have very low fluence. So, angular spread must be accepted

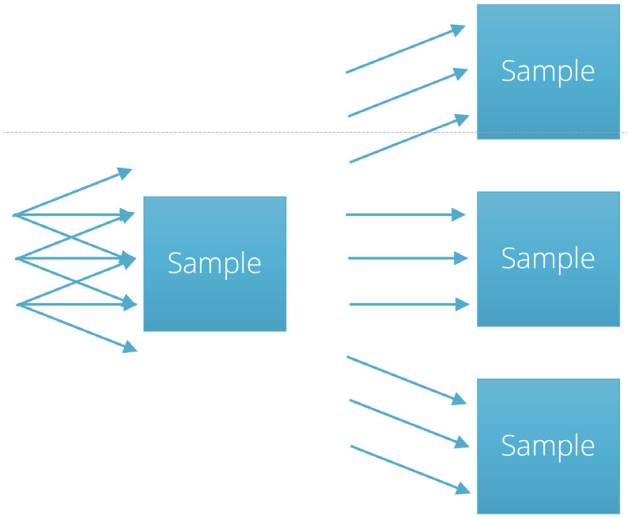

Figure 3-4. The effect of uncollimated source X-rays (i.e. angular spread through the pin-hole) can be rigorously accounted for by superimposing the diffraction patterns produced by multiple incident angles. The broadening here is a result of multiple slightly shifted diffraction patterns with angles associated with the particular hole/slit geometry of a particular source. This contribution produces spot shape corresponding to experiments, rather than pin points.

to improve X-ray source intensity. The angular spread of the incident X-rays is determined by the hole's size, shape and distance from the diode source.

As before, we were able to take advantage of linear superposition to construct an uncollimated diffraction pattern by adding up the contributions from a range of collimated incident angles. The approach is summarized in Figure 3-4. It should be noted that this effective broadening is rigorously calculated by numerical integration of patterns with 0.5 degree resolution. In our experiments, we determined that the slit block allowed ± 1 degree in the spread in the horizontal and ± 0.5 degree in the vertical. This slit geometry was responsible for the elongated diffraction spots in the experiment. Therefore, the angular spread was accounted for by superposition of five collimated beams in the horizontal and three in the vertical. Thus each uncollimated diffraction pattern was constructed from 15 diffraction calculations.

We see from Figure 3-5 that our simulations do much better at capturing the shape and size of the experimental image plate scans when we properly account for the broadening due to the pin hole geometry.

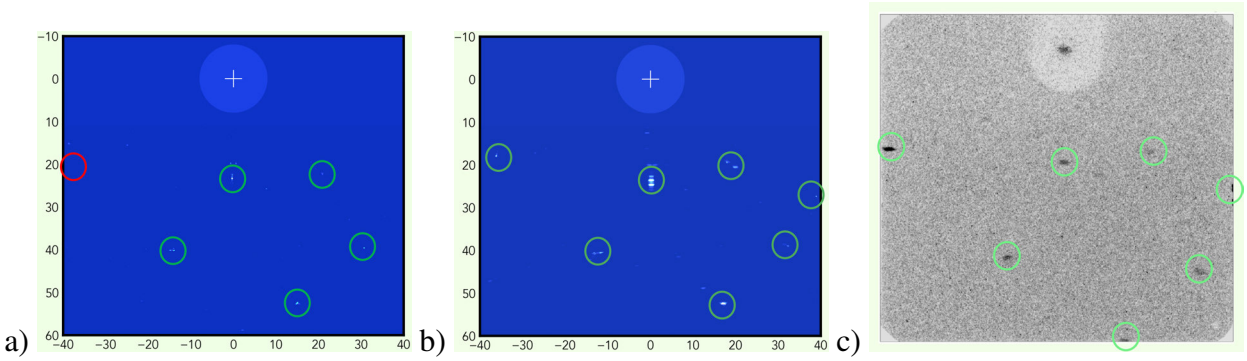

Figure 3-5. Calculated and experimental diffraction patterns. (a) Simulated polychromatic diffraction pattern produced with collimated X-rays (i.e. single incident angle). (b) Simulated polychromatic diffraction pattern numerically integrated to include multiple incident angles corresponding to the angular spread allowed by the pin hole slit. In this case, ± 1 degree in the horizontal and ± 0.5 degree in the vertical. (c) The corresponding experimental diffraction pattern (180° from DICE mark) as seen in Fig. 2-9

3.2.3. *Deformation to Image Plate Geometry*

To this point the simulated diffraction patterns have been plotted in angular coordinates (θ, ϕ), and are therefore shown as projected onto a spherical image plate. But, most experimental image plates are planar. These plates may also be angled with respect to the incident plane.

In order to compare to experimental image plates, we must deform/distort the angular coordinates. The deformations can be thought as a combination of two deformations, as shown in Figure 3-6. The first deformation takes the projection from the sphere to the flat image plane. This is a common deformation, called the mapmaker's deformation for obvious reasons. The second deformation is to account for the tilt of the image plane. This distortion is often referred to as keystoning, and is frequently seen in conference rooms with misaligned portable projectors.

We can combine these two deformations into a single transformation. Here ϕ is the tilt angle. d_{eff} refers to the effective distance between the sample and image plane. In our case, this distance can be scaled to produce the properly sized image in the proper pixel resolution.

The transformation is given by,

$$d_{\text{eff}} = \frac{x_{\text{center}}}{\tan(\phi_{\max})} - (x - x_{\text{center}})\tan(\phi) \tag{3.5}$$

$$x' = x'_{\text{center}} + B\tan^{-1}\left(\frac{(x - x_{\text{center}})}{\sqrt{((y - y_{\text{center}})^2 + d_{\text{eff}}^2)}}\right) \tag{3.6}$$

(3.7)

$$y' = y'_{\text{center}} + B\tan^{-1}\left(\frac{(y - y_{\text{center}})}{d_{\text{eff}}}\right) \tag{3.8}$$

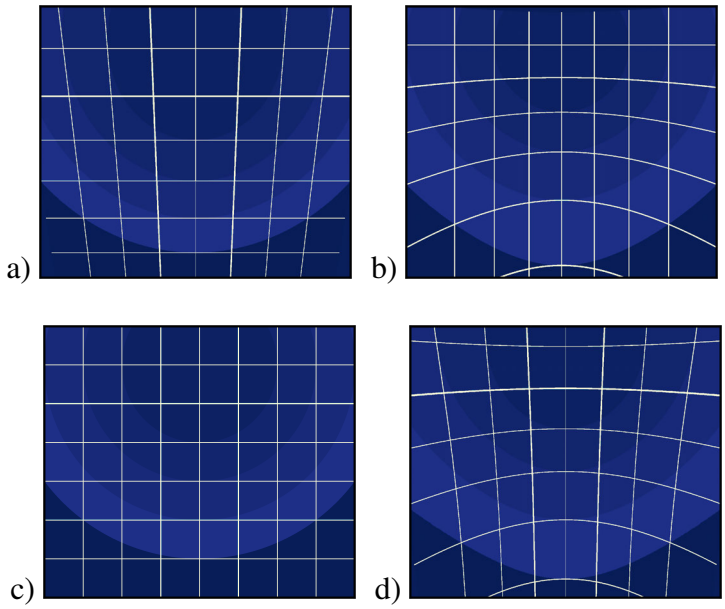

Figure 3-6. Test grid images depicting the deformations produced by projections of a pattern. (a) Depiction of the keystone deformation caused by tilt of an image plate. In this case the tilt is in the vertical. (b) Depiction of the mapmakers projection deformation which results from projecting a grid on a sphere onto a flat surface. (c) Depiction of an undeformed grid as it would appear on a spherical shell image plate. (d) Depiction of the combined keystone tilt and mapmakers projection deformations with a tilt angle of 11 degrees corresponding to the ambient experiments.

where $B = 1146$ is a scaling constant set to give 20 pixels per degree in the horizontal. x' and y' are the final coordinates, and x and y are the initial angular coordinates on a spherical shell.

We see from Figure 3-7 that our simulations do much better at capturing the relative locations of spots in the experimental image plate scans when we properly account for the image plate tilt and shape. This third correction allows for simulations to be overlayed directly on experimental image plate scans.

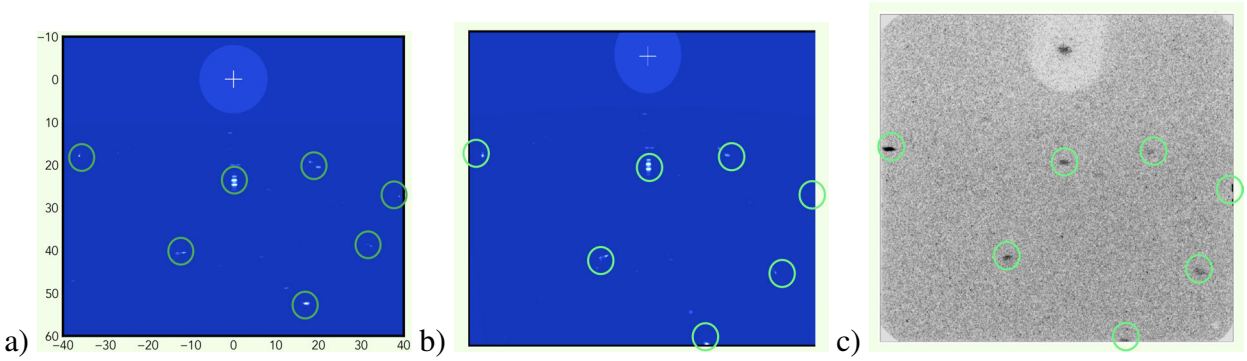

Figure 3-7. Calculated and experimental diffraction patterns. (a) Simulated polychromatic diffraction pattern produced with uncollimated X-rays (i.e. slit hole angular spread) as projected onto a spherical shell image plate. (b) The same simulated polychromatic uncollimated diffraction pattern as it would appear distorted onto a flat image plate tilted relative to the incident angle. In this case, the tilt is 11 degrees, corresponding to the ambient experiments. (c) The corresponding experimental diffraction pattern (180° from DICE mark) as seen in Fig. 2-9

3.3. Application to Experiments

With these significant extensions to the LAMMPS diffraction package, our simulated XRD patterns compare extremely well to experimental image plate scans. Figure 3-7 shows a comparison for the case 180° from DICE mark. In this section we'll show further examples of successful comparison between experiment and simulated XRD patterns. In both ambient pressures and under dynamic compression our simulation tool has proven very useful.

3.3.1. Ambient Pressure Cadmium Sulfide Experimental Comparisons

The first application of our new simulated XRD capability was a validation study based on the ambient pressure experiments described in Chapter 2. In those experiments a sample was placed on a rotating stage with the CdS a-axis pointing upward. A series of 21 diffraction patterns were created in which the sample was rotated through 180 degrees at 10 degree increments. The goal of this validation comparison was to produce good diffraction patterns which agree with each experimental image plane.

One initial difficulty quickly become apparent, as the series of experimental patterns were compared. The bremsstrahlung energy continuum should have lit up a diffraction spot at 2× the 11 degree incident angle. The simulations always showed this spot properly at 22 degrees (2× the incident angle). But in the experiments, the corresponding spot shifted sinusoidally from 19 to 24 degrees through the crystal's rotation. This shift could only be accounted for by a precession of the a-axis (i.e. the crystal's a-axis was not exactly vertical in the rotation stage). Such a misalignment could be caused by error in the crystal growth axis or by imperfect mounting to the stage. Regardless, this observation made clear that the accuracy necessary to match simulated and experimental diffraction patterns was higher than the experimental measurement error.

For the experimental dataset shown in Section 2.2 Figures 2-3 through 2-9, we were able to determine the precession angle which was required to account for the variation - approximately 1.5°. Moreover, with this accounted for, we saw extremely good agreement between simulation and experiments across the dataset. Figure 3-8 shows several examples of the excellent agreement in both spot locations and intensities.

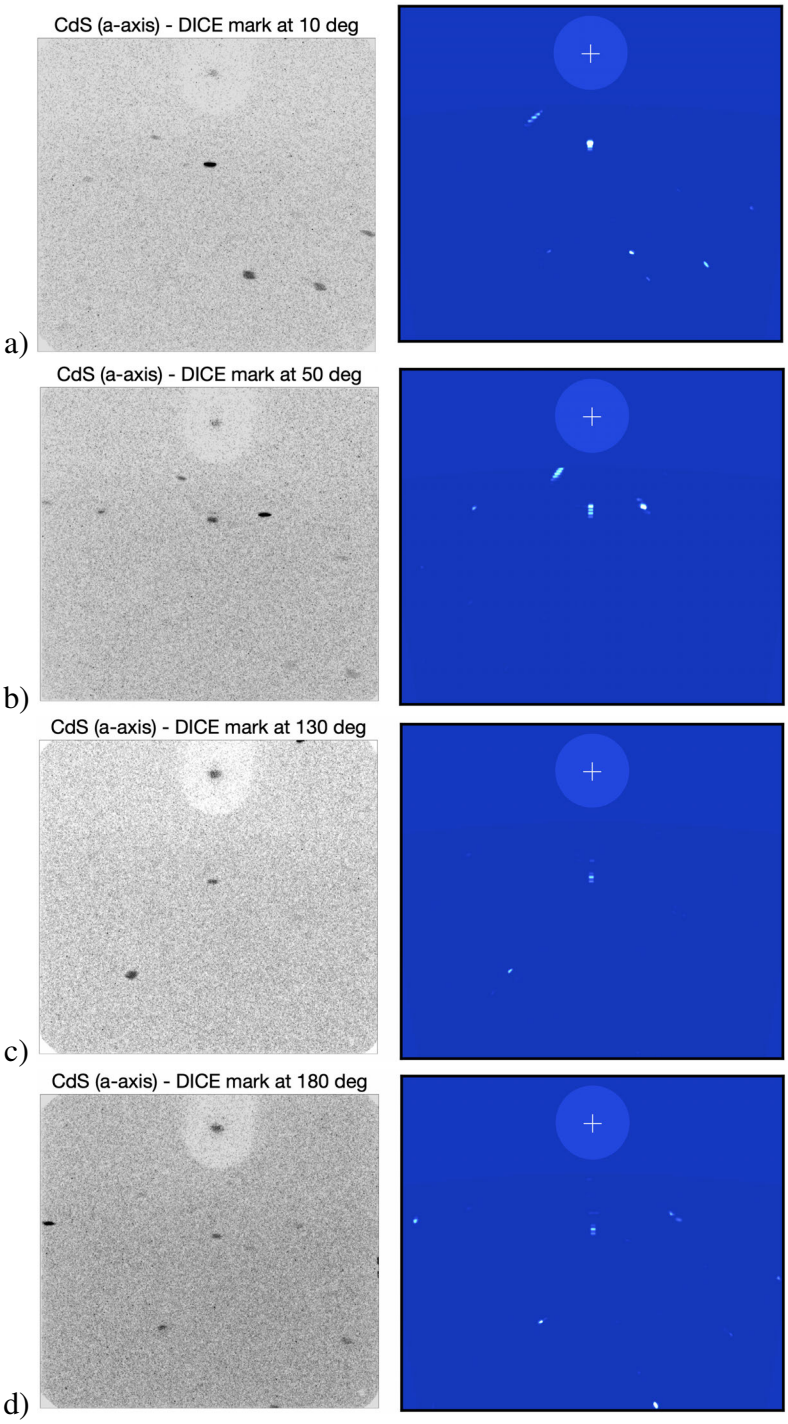

Figure 3-8. Comparison of simulated diffraction patterns with experimental image plates described in Chapter 2. (a) 10°. (b) 50°. (c) 130°. (d) 180°. Agreement is strong both in pattern positions and intensities. Simulations matched the X-ray source energy spectrum, experimental beam/IP geometry and beam angular spread due to slit block.

3.3.2. Dynamic Compression Sector (DCS) Cadmium Sulfide Comparisons

In the ambient pressure experiments we had the luxury of being able to collect data from multiple orientations for a simple sample. In the Thor dynamic experiments we will only be able to shoot one XRD shot per compression. At the Dynamic Compression Sector (DCS) we are able to get up to four shots over a few hundred nanoseconds, but the sample compression continues to evolve between shots. These small experimental datasets will require new analysis methods, using simulated XRD patterns to characterize experiments.

This final section of the chapter described early attempts to use simulation to interpret experiments described earlier in 2.3.

3.3.2.1. High-Pressure c-axis Transition

One of the complications of identification of dynamically compressed final states is the possibility of mixed states. Initial conditions can be carefully chosen to simple single orientations, or homogeneous structures. Final dynamic states, however, can be complex and evolving. The high-pressure mechanism in cadmium sulfide (CdS) is an example. In this case it is known that the mechanism of phase transition from wurtzite to rock salt can produce any of three final orientations. When identifying this final state, one typically identifies the diffraction pattern contributions from each of the three possible single-crystal orientations by comparison with calculated/simulated patterns from these single crystals.

LAMMPS simulations allow an alternative method in which the dynamic compression is simulated and a true mixed state is produced. Since the LAMMPS XRD tools are not limited to single crystals, the combined diffraction pattern can be produced directly from this mixed state. Figure 3-9 shows an example of diffraction patterns produced from dynamically simulated phase transition in CdS. In these simulations, three orientations, oriented 120° with respect to each other are produced. One possible advantage to this approach is that the diffraction pattern from this mixed state may include signatures of the residual deformation and the boundary layers between the various orientations. One disadvantage of this approach is that interatomic potentials must exist which accurately capture the high-pressure behavior at the atomic scale.

These dynamic simulations are not necessary to produce the high-pressure diffraction patterns (i.e. they can instead be manually constructed), however, this capability may be especially useful in evaluating the evolution and heterogeneous states which can be found in dynamic experiments.

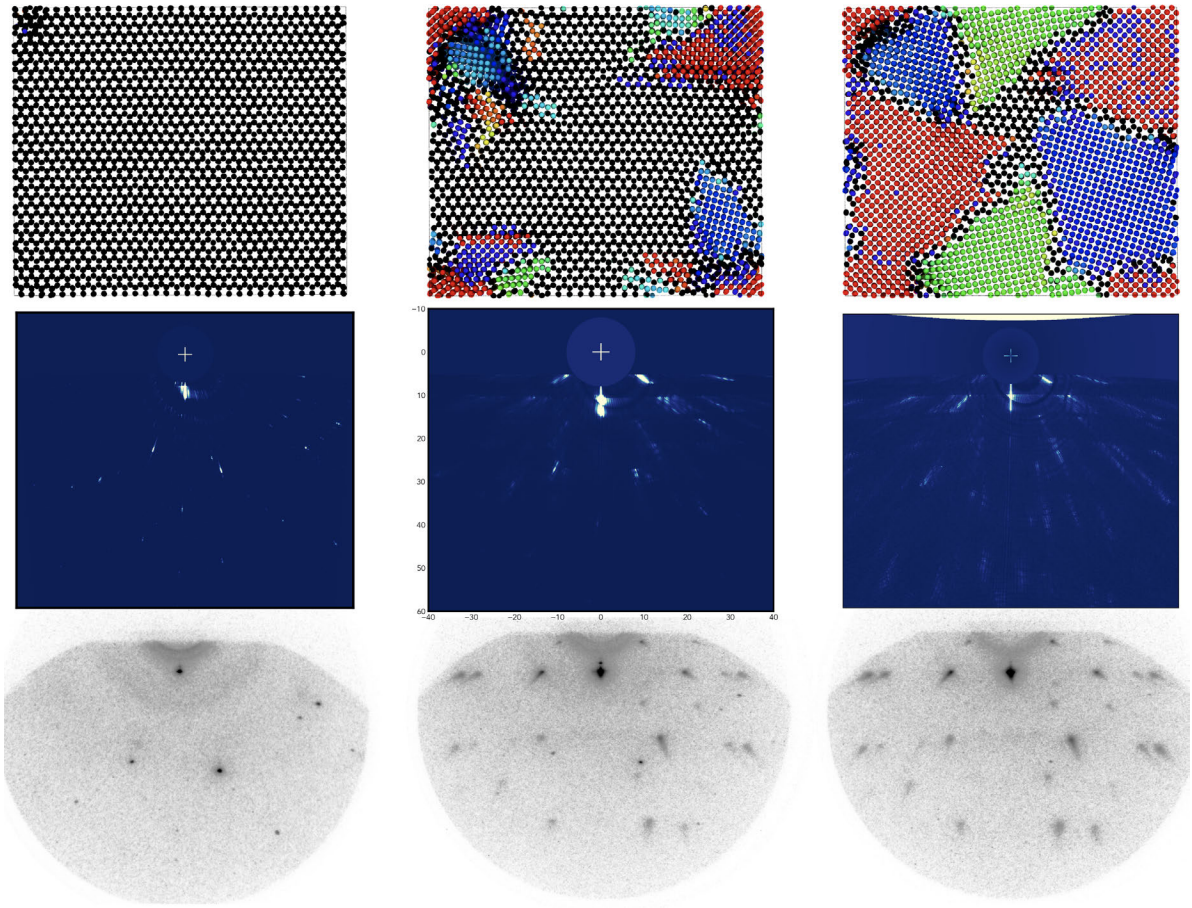

Figure 3-9. Top: Real-space atomistic representations of CdS phase transition under high-pressure (> 5.5 GPa) shock compression colored by lattice type and orientation. Wurtzite is black. Rock salt is green, red or blue, based on orientation. Middle: Simulated diffraction patterns from the atomistic simulations, produced with energy spectrum and angular geometry corresponding to experiments. Because DCS X-rays are highly collimated, a single incident angle was used. Bottom: Experimental patterns showing evolution from wurtzite to rock salt structures. Time progresses from left to right. Experiments correspond with experimental times -43, 110, and 263 ns.

3.3.2.2. Low-Pressure c-axis Transition

The low pressure c-axis transformation in CdS is a good example of an unresolved phase transition mechanism in which simulated x-ray diffraction could prove very useful. At pressures below 5.5 GPa, the c-axis phase transition from wurtzite to rock salt progresses only after an extended incubation time. Moreover, an initial structure appears to develop before the rock salt.

Figure 3-10 shows four experimental XRD images at four times from shot 19-4-074. We see by an overlay of the simulation image that we can clearly identify the initial state of the the -195 ns patterns. At 111 ns, we see the development of a new set of spots highlighted in red. Then at 264 ns, we see the further development of spots highlighted in blue.

While it is computationally intensive to create full diffraction patterns at all possible orientations.

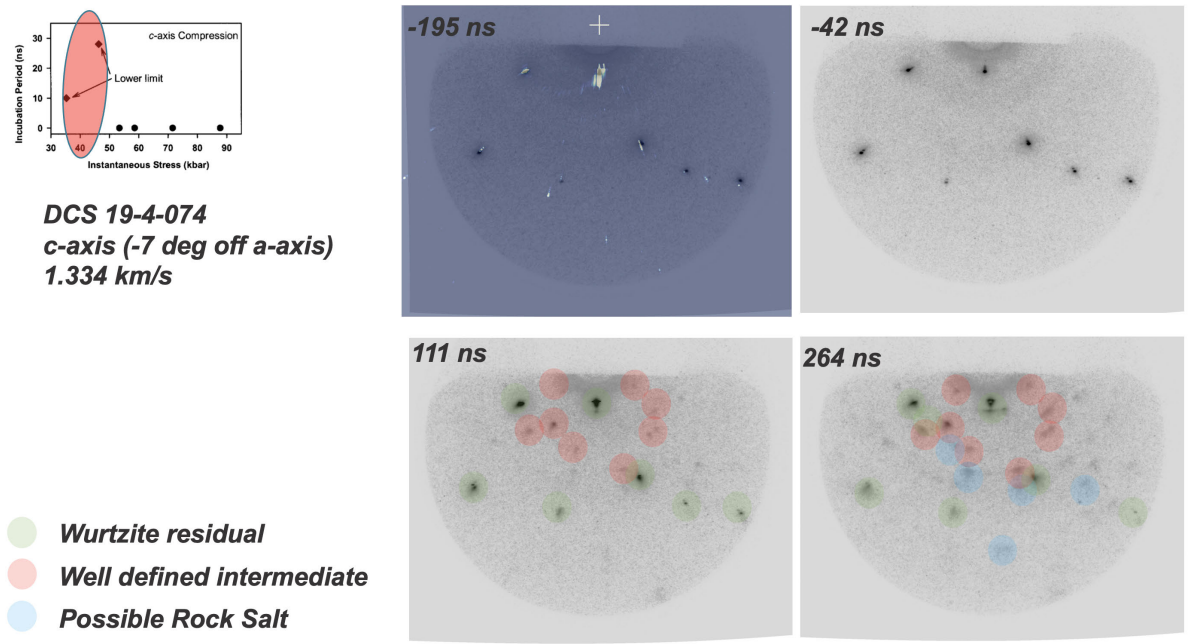

Figure 3-10. DCS experimental results for CdS c-axis compression to low pressures (<5.5 GPa). After an incubation time, new spots are evident, which evolve further with time. These spots are identified as intermediate and ultimately rock salt. The intermediate phase is not consistent with rock salt, which may imply a twinning transition or initial zinc blende phase.

It is possible to observe small areas of the diffraction pattern (i.e. down to even a pixel). Since full diffraction patterns are produced at 1600×1400 resolution, the search of individual pixel intensity can be 10^6 times faster than full diffraction pattern searches. Using this per-pixel search method we were able to distinguish the red-highlighted spots in the intermediate times from the blue-highlighted spots at late time. The blue spots are consistent with possible rock salt configurations. However, the red spots are not. This strongly indicates that the intermediate structure may be a twinning transition or a intermediate structure such as zinc blende, etc.

We term this per-pixel search as a sort of manual "brute-force" approach. We plan to expand on this effort for orientation searches over simulated results in future work. These early successes are exciting, but there are significant further improvements to be made.

While traditional data science approaches to analysis are promising, we are most excited about the application of machine learning methods to our simulated X-ray diffraction data. This will be further explored in Chapter 4.

4. DETERMINING THE ORIENTATION OF THE CRYSTAL LATTICE USING MACHINE LEARNING

4.1. Introduction

Sandia's unique pulsed power capabilities, such as the Z-machine and Thor, dynamically compress matter to extreme states, which enables fundamental analysis of material properties in high-energy density conditions [14]. Specifically, these capabilities transform stored electrical energy into magnetically driven compression force in the orders of 10's and 100's of GPa within nano seconds[14]. X-ray diffraction (XRD) allows for the direct observation of the crystal lattice and as such enables the analysis and characterization of the mechanisms and kinetics that drive/control the compression phenomena with atomistic resolution. Nevertheless, it is important to recognize that analyzing XRD patterns from dynamic compression experiments is not a trivial task for many reasons. First, the X-ray source has broad spectra and can have imperfect collimation. Furthermore, the XRD data generated by dynamic compression experiments is sparse given the fact that it requires for one to perform a Z-machine or Thor shot, which in turn require significant capital expenditure. Consequently, establishing a vast experimental database is intractable. Lastly, noise is present in the obtained patterns from various sources (e.g., window, tamper, machine produced, etc.). Therefore, there is a critical need for enhancing current analysis capabilities of XRD patterns of dynamically compressed materials.

Machine learning is a viable option to enhance current analysis capabilities as these recent works show [38, 39], especially if adequately integrated with computational material science in order to enable the generation of a robust and diverse training set [40]. Furthermore, one can see that Deep Learning (DL) models are a common tool in these recent works [38, 39]. This is unsurprising given the unique and unparalleled ability of these type of models to learn complex non-linear relationships between a set of inputs and a desired set out outputs [41]. However, it can also be seen that recent works focus solely on static compression and on predicting the composition of the materials being analyzed. Nevertheless, these previous successes showcase the tremendous potential for utilizing machine learning to analyze dynamic compression XRD data.

In this report we assess the validity for using machine learning, specifically DL models, for enhancing our current analysis capabilities of XRD data for dynamically compressed data. In this chapter, we provide the details for establishing an accurate model for predicting the orientation of the crystal lattice given XRD pattern image using Convolutional Neural Networks (CNNs). In Chapter 5, we provide the details for removing the noise present in these types of XRD data.

4.2. Theoretical Background on Convolutional Neural Networks

Convolutional Neural Networks (CNNs) are a specific type of deep learning technique capable of learning complex functional mappings between inputs and desired outputs[41]. The underlying architecture of CNNs makes them extremely well suited to establish linkages for inputs that have spatially distributed features such as images (or videos), given their inherent ability to identify in a data-driven manner patterns within the inputs and subsequently link them to the desired outputs. For that reason, CNNs have enjoyed great successes in the computer vision fields for many diverse tasks such as image classification, object localization, and image segmentation [42, 43, 44, 45].

CNNs transform inputs (e.g., images, micrographs, etc.) using a series of different layers to generate a vector or scalar output. A core component of CNNs is the convolutional layer that transform the input by convolving it with a set of filters and subsequently applying a non-linear activation function such as sigmoid or rectified linear unit (ReLU) [46] on the output. A critical characteristic of this layer is that the filters convolved with the image are specifically trained/tailored (by fitting their parameters to a set of training results) to identify salient patterns within the input data that are relevant to the task at hand. As a result, CNNs are an extremely versatile type of deep learning model capable of establishing accurate models across a broad spectrum of disciplines [47, 48, 49, 50].

In this work we will leverage CNNs to establish an accurate model for predicting the orientation of the crystal lattice given an XRD image. Figure 4-1 schematically depicts how a CNN-based model will transform an input XRD image into the desired output. Figure 4-1 shows that the CNN architecture is comprised of a set of convolutional layers and a set of fully-connected layers. The convolutional layers of the CNN architecture identify in a data-driven manner unique patterns within the images. In other words, the set of filters present in the convolutional layers will identify unique fingerprint descriptors within each image to link each image with the desired output. Subsequently, the fully-connected layers transform the identified patterns into the desired outputs. Fully-connected layers are comprised of nodes that transform an input vector x with the following operation:

$$z = f(x^T \beta + b) \tag{4.1}$$

where, β denotes the weights that multiply the input, b represents a bias added to the resultant operation and $f()$ denotes a non-linear activation function. The non-linear activation function allows for non-linear outputs to be generated from the node and a set of nodes applied to the same input forms a fully-connected layer.

The parameters of the model (i.e., the filters and the weights and biases of the fully-connected layers) are fitted to a set of training data that comprised of input-output pairs by minimizing a suitably defined loss (error) function that quantifies the discrepancy between the output predicted by the model and the "true" value from the training data. Typically this minimization protocol is performed using an iterative, non-convex optimization algorithm such as stochastic gradient descent (SGD) [51]. The training of the CNN ends once the loss saturates or it reaches below a pre-established threshold.

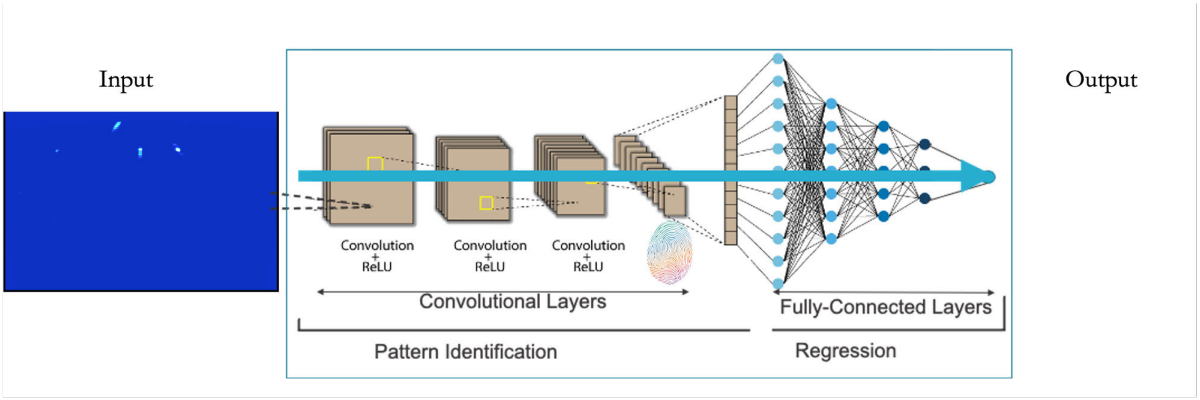

Figure 4-1. Schematic of the implementation of CNNs for the analysis of dynamic XRD patterns.

	Span (°)	Data resolution (°)
Angle #1	0-360	0.5
Angle #2	0-36	4
Angle #3	0-16	4
Angle #4	0-360	180

Table 4-1. Details of the angles sampled with the first training set.

It is important to mention that the learning capacity of CNNs can be further refined by incorporating other types of layers designed for dimensionality eduction (e.g., pooling layer) [41, 42] and normalization [42]. Naturally, the number and type of layer used to define the architecture of the CNN determine the learning capacity of the model. In this work we will explore different architectures in order to establish an accurate linkage between the XRD images and the orientation of the crystal lattice.

4.3. Predicting the orientation angle using Convolutional Neural Networks

In order to establish a linkage between the orientation of the crystal lattice and its corresponding XRD pattern one first needs a diverse and robust set of training data on which the parameters of the CNN-based model are calibrated. For that reason, in this work we first generated a set of synthetic XRD patterns (using the methodology described in Chapter 3) in which the 4 different angles that characterize the orientation of the crystal lattice were varied. Table 4-1 shows the details of the sampled angles with this first training set.

The sampling scheme denoted in Table 4-1 yielded a total of 7195 XRD patterns on which to train a CNN-based model. In order to validate the accuracy of a CNN-based model for predicting the 4 different angles a set of 700 XRD was generated in which the 4 dimensional space defined by Table 4-1 was randomly sampled. Notice that the space defined in Table 4-1 is not the complete set (i.e., 0-360 on each one of the 4 different angles) because trying to determine the validity of a CNN-based model for establishing a linkage in such a large input space will require a

significantly large number of training simulations. For that reason, we decided to first evaluate the validity of these models in a reduced space (i.e., the one defined in Table 4-1).

Our first attempts to link the 4 orientations angles to their corresponding XRD patterns leveraged two state-of-the-art and top-of-the-line image segmentation and classification models that have enjoyed tremendous successes in the image recognition field [52, 53]. The first model used was the VGG model [52], which is a deep CNN with an architecture that leverages very small (3×3) convolution filters to obtain accurate and robust patterns from images. For the specific details of the VGG architecture please reffer to the work of Simonyan et al. [52]. It is important to recognize that the base architecture of VGG was used in this work. Naturally, this means that we modified the input layer to VGG to fit the size of our XRD input images (which are 1601×1401 pixels) as well as the output layer, which we modified to have an output of 4 (i.e., the 4 different angles). The second model used was the Resnet model [53], which stands for residual network. This type of model combines convolutional layers with a residual learning framework in order to learn residual functions (for full details about the method and architecture please refer to [53]). Similarly to the VGG architecture, we modified the input and output layer in order to tailor this powerful architecture for our specific application.

The loss function optimized during training was the mean squared error. In addition, we used a batch size of 5 and a learning rate of 1×10^{-3}. In addition, we leveraged the ADAM optimizer [54] and incorporated a learning rate scheduler that reduced the learning rate by half if the testing loss did not change by 1×10^{-4} over 9 epochs with an initial learning rate of 1×10^{-3}.

Figure 4-2 (a) shows the loss vs. epoch curve for these two different models. It is clear from Figure 4-2 (a) that these two powerful networks are not able to establish a successful model. As a matter of fact, we see that they are severely overfitting to the training data. Consequently, these models are not able to generalize to new/unseen XRD patterns. This is observed from the fact that the training loss decreases rapidly but the testing loss (i.e., XRD patterns that the model has not been trained on) yield a high value of the loss. Consequently, a robust and accurate linkage was not able to be established even with these powerful architectures.

Therefore, in order to determine if it is viable/possible to leverage CNN-based models to predict the orientation of the crystal lattice we trained the VGG architecture and the Resnet architecture on a simplified dataset in which solely the first angle was varied from 0° to 360° with a resolution of 0.5° while keeping the remaining three angles constant. As a result, this new simplified dataset now consists of 720 XRD training patterns. The ability of the model to generalize to new/unseen patterns will be assessed with a test set that was generated by randomly sampling 296 angles between 0° and 360°.

We trained Resnet and VGG on the simplified dataset using the same procedure, optimizers, batch size, learning rate and learning rate schedule as before. Figure 4-2 (b) shows the loss vs. epoch curve for the VGG and the Resnet architectures on the simplified dataset. Unfortunately, 4-2 (b) also shows that these two powerful models are not able to establish an accurate model given the fact that it is still observed that the Resnet architecture overfits to the training set (observe the rapid decrease and low value of the training loss compared to the testing loss). However, now it is observed that the VGG architecture is not able to learn at all since the training loss and the testing loss still have a large value but they are similar.

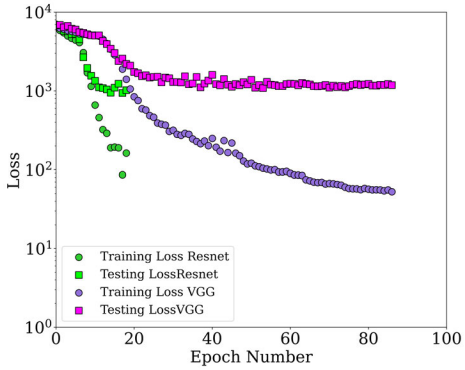

(a) Loss evolution curve for predicting the 4 orientation angles without considering symmetry.

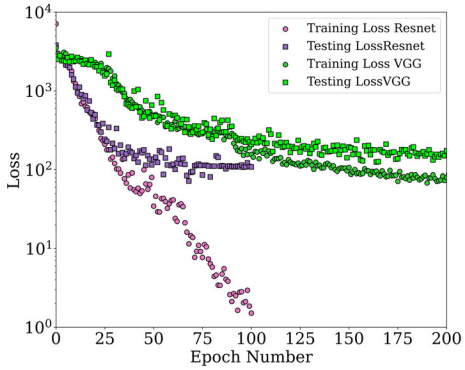

(b) Loss evolution curve for predicting the first orientation angle without considering symmetry.

Figure 4-2. Loss evolution plots for a direct implementation of CNN-based models for predicting the orientation of the crystal lattice.

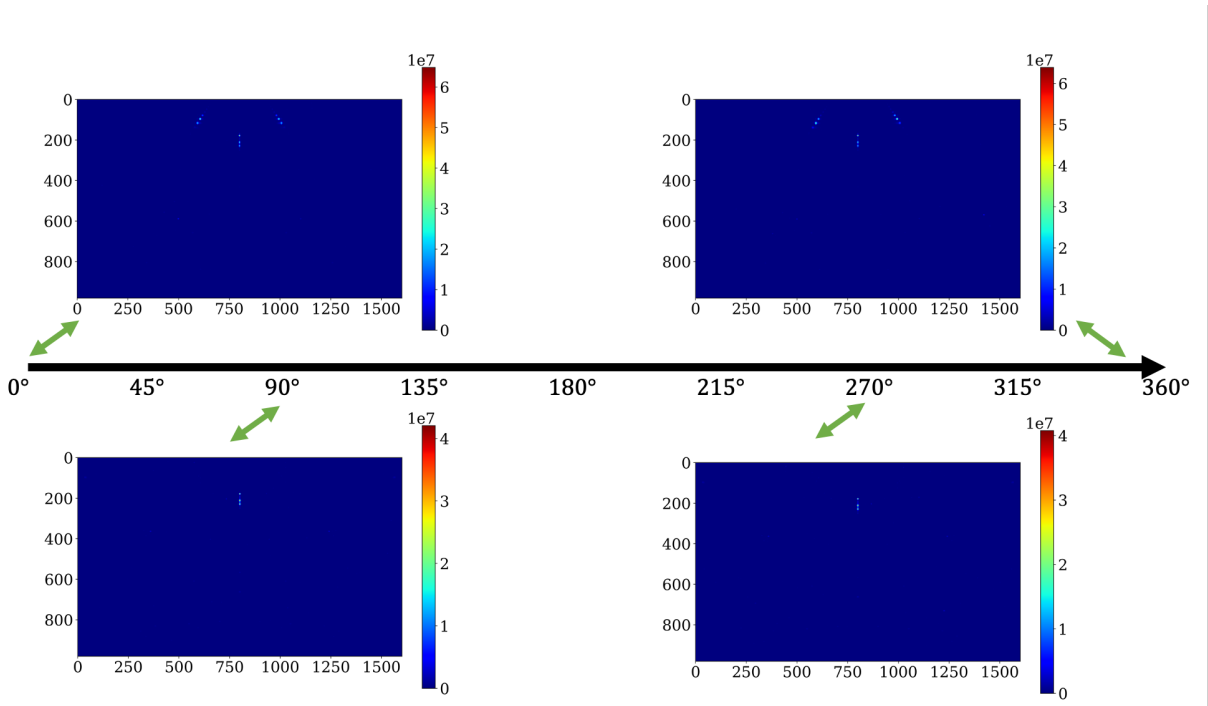

Figure 4-3. Schematic Showing the Symmetry present in the simplified dataset in which solely the first angle was varied.

Consequently, Figure 4-2 (a) and (b) demonstrate that a direct implementation of CNN-based models is not capable to establish a linkage between the orientation and its corresponding XRD pattern. Therefore, this means that appropriate consideration of the physical properties needs to be accounted if one is going to establish an accurate model. Lattice orientations have symmetries present and Figure 4-3 schematically depicts the symmetries present in the simplified dataset in which solely the first angle was varied and it is clearly observed that symmetry exists with respect to 180°. Therefore, this explains why previous attempts, shown in Figure 4-2 (a) and (b), were unsuccessful. The main reason is that the symmetries present in the data cause for two different sets of angles to have similar XRD patterns. Consequently, the networks on their own were not able to learn a robust linkage. Notice that in the case in which the 4 angles were varied identifying the symmetries is not as trivial as the simplified dataset, which only required for one to plot the different patterns to identify the symmetry. As a matter of fact, identifying the symmetries in the space defined by the 4 angles requires using data-driven techniques that will be addressed in future work. For that reason, in this work we will solely focus in determining the validity of CNN-based models for establishing a linkage for the simplified dataset.

Therefore, we accounted for the symmetry present in the XRD patterns by replacing the value of any angle greater than 180° with the value of 360° minus the angle being replaced. Therefore, using this transformation we can see that the angles shown in Figure 4-3 now have the same values. Furthermore, we normalized the value of each angle by the maximum value (i.e., 180° when accounting for symmetry) in order to transform the value of the output to the domain 0-1, which aids in convergence and performance of deep learning models. Also, following typical implementations of deep learning models we transformed the inputs (i.e., the XRD patterns) by

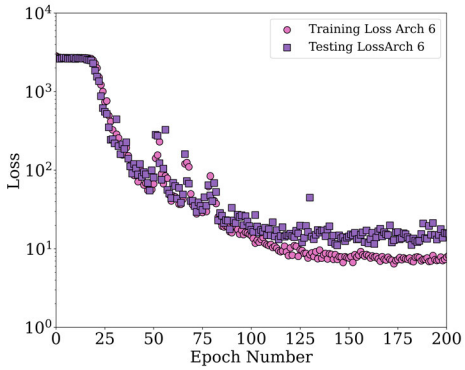

Figure 4-4. Loss evolution curve for predicting the first orientation angle considering symmetry.

removing the median value and scaling it according to the interquartile range.

Now that the output values on which the model will be trained account for symmetry and the inputs that the model will transform into the desired outputs have properties that enable better performance, we decided to use a simpler architecture rather than the complex (yet powerful) VGG and Resnet architectures. The simpler architecture consists of 4 convolutional layers and two fully-connected layers. The first convolutional layer has 4 output channels and implements convolutional filters of size 10×10. Also, the first convolutional layer applies a pooling layer with kernel size 10 and stride 10 and a batch normalization layer. A rectified linear unit (ReLU) activation function is applied after the first layer. The second convolutional layer also applies convolutional filters of size 10×10 but has 8 output channels (instead of 4) and also applies a pooling layer (with the same kernel size and stride as the first layer) and a batch normalization layer. In a similar manner, a ReLU activation function is applied after the second layer. The third convolutional layer has 16 output channels and applies convolutional filters of size 5×5 and does not apply a pooling layer but it does apply a batch normalization layer followed by a ReLU activation function. The fourth and final convolutional layer is exactly the same as the third layer, meaning that it applies convolutional filters of size 5×5, followed by a batch normalization layer and a ReLU activation function. As stated previously, following the convolutional layers we applied two fully connected layers. The first fully connected layer has 32 nodes followed by a ReLU activation function and the final fully connected layer regresses the 32 features into the value of the angle. Finally, in order to ensure that the value is between 0 and 1 (recall that we transformed the values of the output to this range) we apply a sigmoid activation function after the final fully connected layer. We trained this architecture using the same procedure, optimizers, batch size and learning rate as the Resnet and VGG architectures.

Figure 4-4 shows the loss vs. epoch curve for the simplified CNN architecture and it can be clearly seen that the network is indeed training and not overfitting to the training set since the training and testing loss have similar values. In order to further analyze the validity and accuracy of the simplified CNN architecture we compared the predicted values of the angles to the ground truth values. Figure 4-5 (a) shows the scatter plot of the true values vs the predicted values and demonstrates that the simplified CNN architecture is quite accurate since all the points in the plot

lie close to the diagonal (i.e., a perfect prediction). Figures 4-5 (b) and (c) further demonstrate this point since they show that the probability density of the predicted values for both the training and testing set is quite similar to that one of the true values.

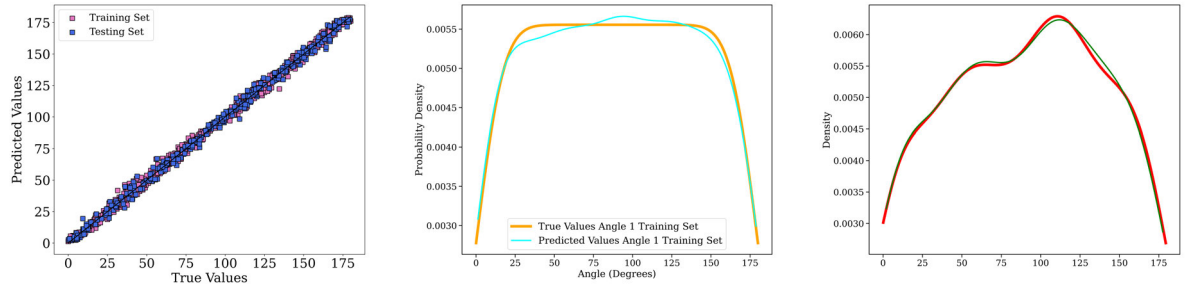

(a) Scatter plot true vs. predicted of the first angle using CNN-based model that considers symmetry .

(b) Probability densities of the true and predicted values of the training set the first angle using CNN-based model that considers symmetry.

(c) Probability densities of the true and predicted values of the test set the first angle using CNN-based model that considers symmetry.

Figure 4-5. Performance of CNN-based model that considers symmetry for predicting the value of the first orientation angle .

As a result, Figures 4-4 and 4-5 demonstrate that by adequately accounting for the symmetry present in the XRD patterns (caused by the crystallographic nature of the lattice) and performing appropriate transformations on the inputs and outputs of the model a simple CNN-based model was capable of accurately predicting the orientation of the crystal lattice.

Now we can determine the level of resolution (i.e., the number of samples) with which a CNN-based model can establish an accurate model by training and evaluating the performance of the simple CNN-architecture on different training sets. Figures 4-4 and 4-5 demonstrated that a training set with a resolution of 0.5° is capable of establishing an accurate model. Therefore, we will now systematically sample the input domain of the first angle (0° to 360°) with fewer number of samples. Specifically, we evaluated 5 different resolutions, each one sampling the input domain with half of the points as the previous one. In other words, the first training set had a 1° resolution, the second training set has a resolution of 2°, the third one has a resolution of 4°,the fourth one has a resolution of 8° and the fifth training has a resolution of 16°. Subsequently, we trained the simple CNN architecture using the same optimizer, learning rate, learning rate scheduler and batch size as before for 200 epochs. Figures 4-6 shows the scatter plot of the true vs. predicted values for the 5 different training sets used and it clearly shows that a resolution of 0.5° yields the best model. However, it is interesting to point out the progressive decrease in accuracy as the sampling of the first degree is decreased. Figures 4-6 (a) and (b) show that a model is able to be established, meaning that the CNN-based model was able to learn a linkage though quite inaccurate. Figures 4-6 (c) shows that the model was not able to learn at all since it simply predicts the same value of the first angle for all the XRD patterns. Lastly, Figures 4-6 (d) and (e) show that the model essentially memorizes the training set and is unable to generalize to any new/unseen XRD patterns.

As discussed previously, a CNN-based model identifies in a purely data-driven and automatic manner patterns within an image (in the case of this work an XRD image) that are most correlated to the desired outputs by applying successive convolutional filters (whose weights are determined during the training of the model). In our initial success we used an XRD image pattern of 1601×1401 pixels. However, one might be able to establish an accurate model with a smaller resolution. Therefore, we trained the same simple CNN-based architecture to three different datasets in which we systematically reduced the resolution of the XRD image patterns. The first dataset had a resolution of 533×467, the second dataset had a resolution of 320×280 and the third and final dataset had a resolution of 160×140.

Figures 4-7 shows the scatter plot of the true vs. predicted values for the three different training sets used and it clearly shows that a full resolution XRD image of 1601×1401 was not necessary for a CNN-based model to identify robust patterns within the XRD images and establish an accurate and successful model. As a matter of fact Figures 4-7 (b) shows that an accurate model can be established with XRD images with a resolution of 320×280 pixels. Lastly,Figures 4-7 (c) shows that reducing the resolution thus indeed affect the model performance.

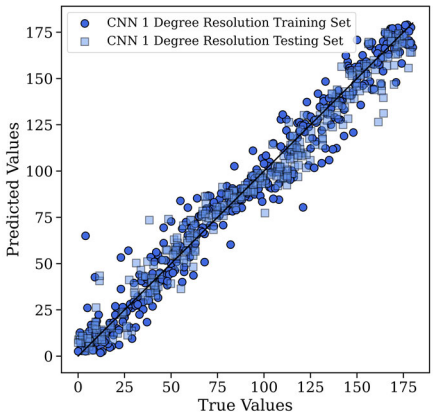

(a) Degree 1.

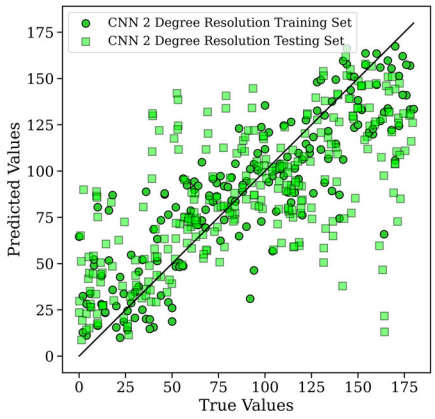

(b) Degree 2.

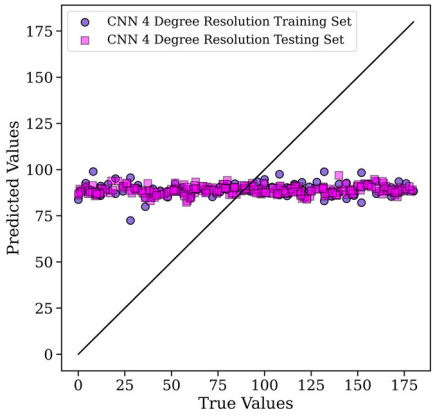

(c) Degree 4.

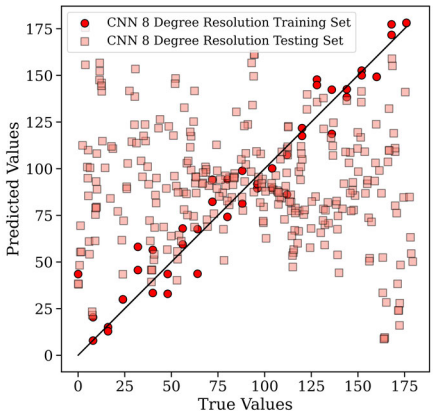

(d) Degree 8.

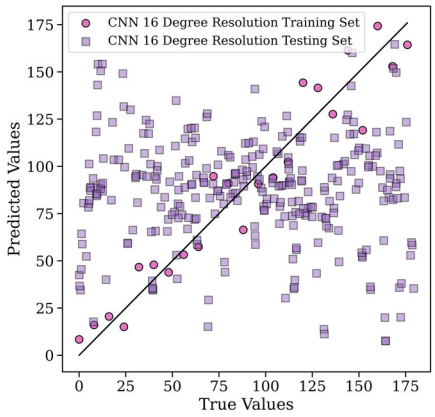

(e) Degree 16.

Figure 4-6. Scatter plots of true vs. predicted values for different degree resolutions.

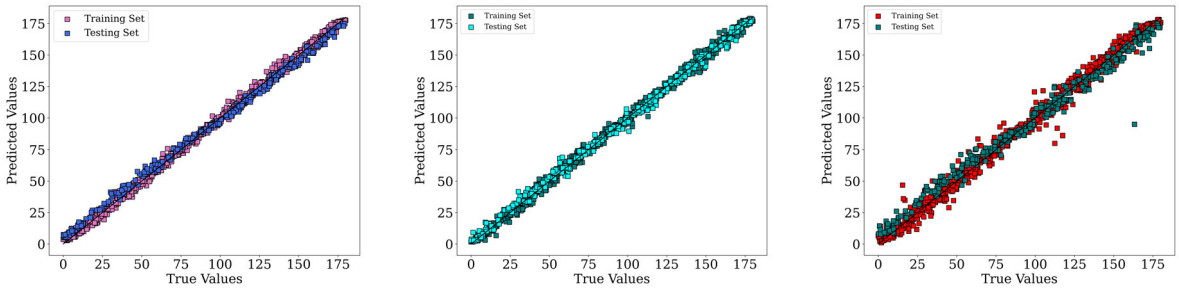

(a) Scatter plot of model trained with 533×467 pixel XRD patterns .

(b) Scatter plot of model trained with 320×280 pixel XRD patterns.

(c) Scatter plot of model trained with 160×140 pixel XRD patterns.

Figure 4-7. Scatter plots of the same CNN-based model trained on XRD images with systematically lower resolution.

5. MACHINE LEARNING DENOISING OF EXPERIMENTAL DATA

5.1. Leveraging Deep Learning to de-noise experimentally obtained XRD patterns.

In this section we leverage deep learning (DL) to separate the diffraction signal from noise of experimentally obtained XRD patterns. For specific details of the experimentally obtained XRD patterns please refer to Chapter 2. Recently, DL methods have enjoyed significant success in the computer vision and image segmentation field [55] given their unique ability to learn complicated relationships [41]. Specifically, Convolutional Neural Networks (CNNs) have shown great promise and success in this area thanks to their unparalleled capacity for uncovering relationships within input data with spatially distributed features, such as images or video, in an automated and data-driven manner [41, 56]. Furthermore, by adequately incorporating uncertainty quantification[57, 58] into CNNs one is now capable of establishing models that provide a distribution of predictions of segmented images, which in turn allows for the adequate consideration of uncertainty in the segmentation process.

The DL-based model used to separate the relevant data from the noise that is present on the experimentally obtained XRD patterns was a U-net architecture [56] specially tailored in previous work to account for uncertainty by using Monte Carlo dropout[57, 58] . The work of Roberts et al. [57] provides specific details about the architecture of the model used and the methodology for incorporating uncertainty into DL-based image segmentation models.

The DL-based model was trained on 20 different experimentally obtained XRD patterns and it provides a prediction for a new XRD pattern by classifying each pixel in the XRD image as either noise or not noise. In order for the model to be able to provide an accurate prediction it leverages domain-expertise guided segmentation in addition to the experimental patterns. For the case of this work, a segmented label was obtained for each of the 20 different patterns by first applying a median denoising filter to reduce background noise. After this, grayscale intensity thresholding was performed to obtain our final labels. These labels were then used to provide the DL-based model with examples of the desired segmentation and its fidelity.

Once the model is trained, it provides a distribution of predictions for each pixel (using Monte Carlo dropout). Thus, enabling the DL-model to also account for uncertainty in the prediction of the class of each pixel [57]. Subsequently, the model enhances the prediction by classifying as noise the pixels that show the highest uncertainty. Lastly, a final prediction is made by leveraging traditional image processing methods to fill gaps in the pixel clusters identified as relevant data. Specifically, we use the `binary_dilation` and `binary_erosion` functions from the Scikit-image library's `morphology module` [59]. As a result, by adequately leveraging Monte Carlo dropout and integrating it with traditional image processing methods we are able to obtain an accurate and robust segmentation.

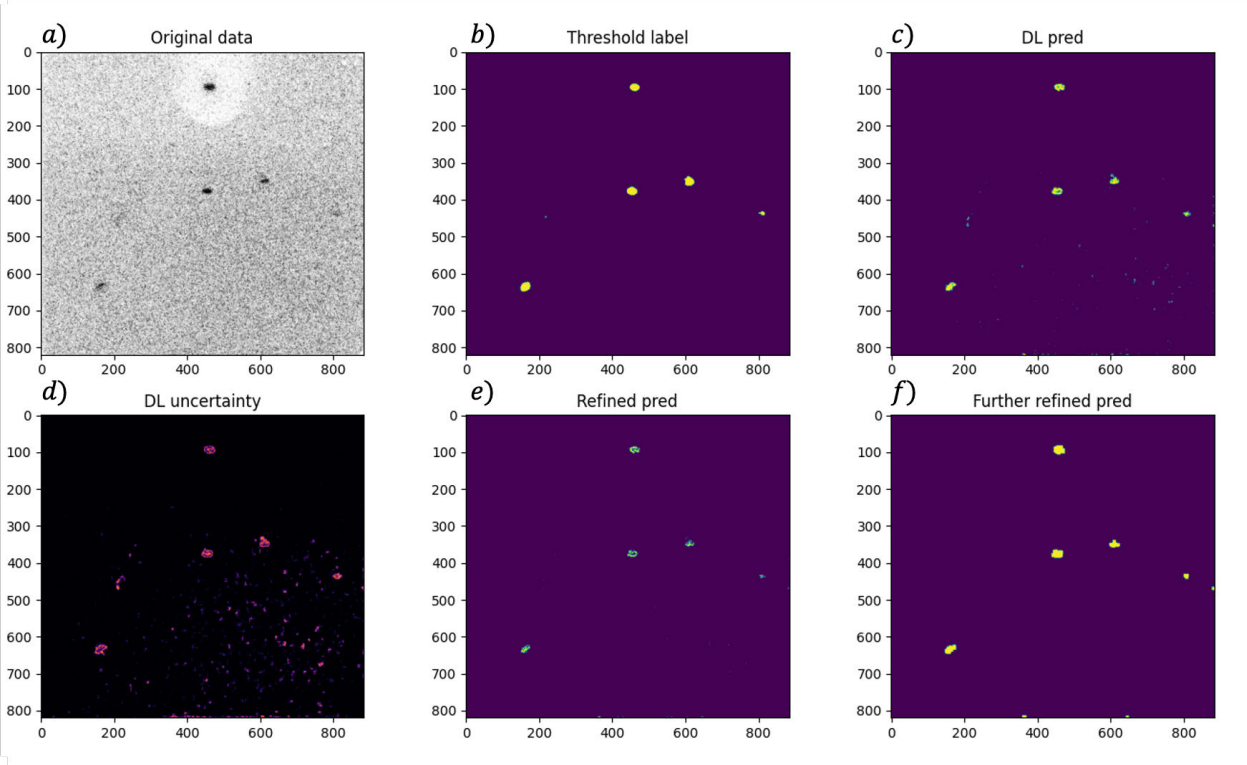

Figure 5-1. Segmentation results obtained using a U-NET based de noising model that accounts for uncertainty.

Figure 5-1 shows the segmentation results of using the DL-based segmentation algorithm introduced earlier in this section. Figure 5-1 (a) shows the original image and Figure 5-1 (b) shows the expert label that the model used to segment the data. Figure 5-1 (c) shows the resultant DL-based prediction of the segmented image. Figure 5-1 (d) shows the probability map with which the DL-based model accounts for the uncertainty, Figure 5-1 (e) shows a refined prediction using the information obtained with the probability map (i.e., the uncertainty). The refined segmentation shown in Figure 5-1 (e) was obtained by classifying as noise the pixels that showed the highest uncertainty. Nevertheless, notice that this causes the prediction shown in Figure 5-1 (e) to have gaps within the clusters for pixels that have not been classified as noise. For that reason, Figure 5-1 (f) shows a further refined segmentation were the gaps in the image were filled using traditional image processing methods (e.g., dilation/erosion techniques).

As it can be seen from Figure 5-1 the DL-based model trained in this section successfully learned to separate diffraction signal from noise given 20 training examples with labels provided by a subject matter expert.

6. CONCLUSIONS AND FUTURE WORK

This one-year LDRD was very successful in establishing a basic simulated XRD capability, proving the concept of machine learning image analysis, and applying these new tools to experimental data. We are very excited to be able to extend this research project to a new three-year LDRD in FY23. This new project allows us to mature and extend our current work to increase the impact of this new capability.

We accomplished several specific goals this year. Specifically, we were able to code and validate new LAMMPS tools for 2D XRD pattern creation. We were able to produce CdS 2D XRD training data for wurtzite and rock salt structures. We were able to augment this code with advanced calculation capabilities, e.g. broad X-ray spectrum. Moreover, we completed training of machine learning pattern recognition models (CNN-based) for single crystal CdS. And, we demonstrated noise filtering models trained from Thor experimental data. Finally, we were able to apply these new tools to ambient and dynamic experiments.

In FY2022, we were able to communicate recent findings from this LDRD (SimXRD) and our recent LDRD 213088 (ThorXRD). This included two peer-reviewed publications and five conference presentations.

Peer-reviewed Publications

1. T. Ao, D. Morgan, B. Stoltzfus, K. Austin, J. Usher, E. Breden, L. Pacheco, S. Dean, J. Brown, S. Duwal, H. Fan, P. Kalita, M. Knudson, J.M.D. Lane, "A Compact X-ray Diffraction System for Dynamic Compression Experiments on Pulsed-power Generators," *Rev. Sci. Instrum.*, **93**:053909, 2022.

2. David Montes de Oca Zapiain, Dane V. Morgan, Bryce A. Thurston, Tommy Ao, Mark A. Rodriguez, Marcus Knudson, J. Matthew D. Lane, "Simulated X-ray Diffraction and Machine Learning for Interpretation of Dynamic Compression Experiments," *AIP Conf. Proc.*, (to be submitted)

Invited and Contributed Presentations

1. "Phase Transition Mechanisms in Cadmium Sulfide from X-ray Diffraction Comparisons of High-pressure Experiments and Molecular Dynamics Simulation," J Matthew D Lane, Bryce A Thurston, Tommy Ao, David Montes de Oca Zapiain, Mark A Rodriguez, Marcus D Knudson. APS March Meeting, Mar 2022, Chicago IL.

2. “X-ray diffraction of materials under ramp compression on the Thor pulsed-power generator,” Tommy Ao, Dane V Morgan, J Matthew D Lane, Kevin N Austin, Eric W Breden, Justin L Brown, Sakun Duwal, Hongyou Fan, Patricia Kalita, Marcus Knudson, Lena M Pacheco, Mark A Rodriguez, Brian S Stoltzfus, Joshua M Usher. APS Shock Compression of Condensed Matter Conf., Jul 2022, Anaheim CA.
3. “Simulated X-ray Diffraction and Machine Learning for Interpretation of Dynamic Compression Experiments,” David Montes de Oca Zapiain, Dane V Morgan, Bryce A Thurston, Tommy Ao, Mark A Rodriguez, Marcus Knudson, J Matthew D Lane. APS Shock Compression of Condensed Matter Conf., Jul 2022, Anaheim CA.
4. “Transformation mechanisms for the pressure-induced phase transition in single crystal CdS” Marcus Knudson, Dane V Morgan, Tommy Ao, Mark A Rodriguez, David Montes de Oca Zapiain, J Matthew D Lane. APS Shock Compression of Condensed Matter Conf., Jul 2022, Anaheim CA.
5. “Simulated X-ray Diffraction and Machine Learning for Interpretation of Dynamic Compression Experiments,” David Montes de Oca Zapiain, Dane Morgan, Bryce Thurston, Tommy Ao, Brendan Donohue, Carianne Martinez, Mark A. Rodriguez, Marcus D. Knudson, and J. Matthew D. Lane , Jul 2022, Sandia ML/DL Workshop

Looking forward we aim to make several improvements to the XRD simulation tool, including the incorporation of c/a distortion, automated peak labeling, efficiency improvements, and a user interface. For the machine learning, we will be extending our orientation determination algorithm to full orientation angles, developing transfer tools between simulated and experimental data, incorporating active learning approaches to extract symmetries, and generalizing the approach to powder samples.

This year our focus has been on computation, but going forward, we would like to actively incorporate experiments and new data in CdS, Bismuth and especially tamper materials like LiF and TPX. These experiments will initially focus of dynamic platforms such as Thor and DCS. However, we aim to move to include high-fidelity powder characterization and calibration through the Rodriguez lab.

Through new features, new models and new applications we aim to significantly extend the efficiency, usability and impact of these new simulated analysis tools.

REFERENCES

[1] S.C. Jones and Y.M. Gupta. Impact surface VISAR measurements in CdS shocked along the c-axis. *AIP Conf. Proc.*, 505:105–108, 2000.

[2] L. M. Barker and R. E. Hollenbach. Laser interferometer for measuring high velocities of any reflecting surface. *J. Appl. Phys.*, 43:4669–4675, 1972.

[3] O. T. Strand, D. R. Goosman, C. Martinez, T. L. Whitworth, and W. W. Kuhlow. Compact system for high-speed velocimetry using heterodyne techniques. *Rev. Sci. Instrum.*, 77:083108, 2006.

[4] Stefan J. Turneaure, Surinder M. Sharma, and Y. M. Gupta. Nanosecond melting and recrystallization in shock-compressed silicon. *Phys. Rev. Lett.*, 121:135701, Sep 2018.

[5] J. R. Rygg, J. H. Eggert, A. E. Lazicki, F. Coppari, J. A. Hawreliak, D. G. Hicks, R. F. Smith, C. M. Sorce, T. M. Uphaus, B. Yaakobi, and G. W. Collins. Powder diffraction from solids in the terapascal regime. *Rev. Sci. Instrum.*, 83:113904, 2012.

[6] A. E. Gleason, C. A. Bolme, E. Galtier, H. J. Lee, E. Granados, D. H. Dolan, C. T. Seagle, T. Ao, S. Ali, A. Lazicki, D. Swift, P. Celliers, and W. L. Mao. Compression freezing kinetics of water to ice VII. *Phys. Rev. Lett.*, 119:025701, 2017.

[7] Damian C. Swift. X-ray diffraction from shock-loaded polycrystals. *Rev. Sci. Instrum.*, 79:013906, 2008.

[8] Patricia Kalita, Paul Specht, Seth Root, Nicholas Sinclair, Adam Schuman, Melanie White, Andrew L. Cornelius, Jesse Smith, and Stanislav Sinogeikin. Direct observations of a dynamically driven phase transition with in situ X-Ray diffraction in a simple ionic crystal. *Phys. Rev. Lett.*, 119:255701, Dec 2017.

[9] Daniel H. Kalantar, E. Bringa, M. Caturla, J. Colvin, K. T. Lorenz, M. Kumar, J. Stölken, A. M. Allen, K. Rosolankova, J. S. Wark, M. A. Meyers, M. Schneider, and T. R. Boehly. Multiple film plane diagnostic for shocked lattice measurements (invited). *Rev. Sci. Instrum.*, 74:1929–1934, 2003.

[10] Matthew Suggit, Giles Kimminau, James Hawreliak, Bruce Remington, Nigel Park, and Justin Wark. Nanosecond X-ray laue diffraction apparatus suitable for laser shock compression experiments. *Rev. Sci. Instrum.*, 81:083902, 2010.

[11] Dominik Kraus, A Ravasio, M Gauthier, DO Gericke, J Vorberger, S Frydrych, J Helfrich, LB Fletcher, G Schaumann, B Nagler, B. Barbrel, B. Bachmann, E. J. Gamboa, S. Gode, E. Granados, G. Gregori, H. J. Lee, P. Neumayer, W. Schumaker, T. Doppner, R. W.

Falcone, S. H. Glenzer, and M. Roth. Nanosecond formation of diamond and lonsdaleite by shock compression of graphite. *Nature Communications*, 7:1–6, 2016.

[12] P. A. Rigg and Y. M. Gupta. Time-resolved X-ray diffraction measurements and analysis to investigate shocked lithium fluoride crystals. *J. Appl. Phys.*, 93:3291–3298, 2003.

[13] B. J. Jensen and Y. M. Gupta. Time-resolved X-ray diffraction experiments to examine the elastic-plastic transition in shocked magnesium-doped lif. *J. Appl. Phys.*, 104:013510, 2008.

[14] T. Ao, M. S. Schollmeier, P. Kalita, P. D. Gard, J. R. Williams, C. B. Blada, H. L. Hanshaw, I. C. Smith, J. E. Shores, C. S. Speas, and C. T. Seagle. X-ray diffraction of dynamically compressed matter on Sandia's Z Pulsed Power Facility. Technical Report SAND2019-11868, Sandia National Laboratories, 2019.

[15] D. B. Sinars, M. A. Sweeney, C. S. Alexander, D. J. Ampleford, T. Ao, J. P. Apruzese, C. Aragon, D. J. Armstrong, K. N. Austin, T. J. Awe, A. D. Baczewski, J. E. Bailey, K. L. Baker, C. R. Ball, H. T. Barclay, S. Beatty, K. Beckwith, K. S. Bell, J. F. Benage, N. L. Bennett, K. Blaha, D. E. Bliss, J. J. Boerner, C. J. Bourdon, B. A. Branch, J. L. Brown, E. M. Campbell, R. B. Campbell, D. G. Chacon, G. A. Chandler, K. Chandler, P. J. Christenson, M. D. Christison, E. B. Christner, R. C. Clay, K. R. Cochrane, A. P. Colombo, B. M. Cook, C. A. Coverdale, M. E. Cuneo, J. S. Custer, A. Dasgupta, J.-P. Davis, M. P. Desjarlais, D. H. Dolan, J. D. Douglass, G. S. Dunham, S. Duwal, A. D. Edens, M. J. Edwards, E. G. Evstatiev, B. G. Farfan, J. R. Fein, E. S. Field, J. A. Fisher, T. M. Flanagan, D. G. Flicker, M. D. Furnish, B. R. Galloway, P. D. Gard, T. A. Gardiner, M. Geissel, J. L. Giuliani, M. E. Glinsky, M. R. Gomez, T. Gomez, G. P. Grim, K. D. Hahn, T. A. Haill, N. D. Hamlin, J. H. Hammer, S. B. Hansen, H. L. Hanshaw, E. C. Harding, A. J. Harvey-Thompson, D. Headley, M. C. Herrmann, M. H. Hess, C. Highstrete, O. A. Hurricane, B. T. Hutsel, C. A. Jennings, O. M. Johns, D. Johnson, M. D. Johnston, B. M. Jones, M. C. Jones, P. A. Jones, P. E. Kalita, R. J. Kamm, J. W. Kellogg, M. L. Kiefer, M. W. Kimmel, P. F. Knapp, M. D. Knudson, A. Kreft, G. R. Laity, P. W. Lake, D. C. Lamppa, W. L. Langston, J. S. Lash, K. R. LeChien, J. J. Leckbee, R. J. Leeper, G. T. Leifeste, R. W. Lemke, W. Lewis, S. A. Lewis, G. P. Loisel, Q. M. Looker, A. J. Lopez, D. J. Lucero, S. A. MacLaren, R. J. Magyar, M. A. Mangan, M. R. Martin, T. R. Mattsson, M. K. Matzen, A. J. Maurer, M. G. Mazarakis, R. D. McBride, H. S. McLean, C. A. McCoy, G. R. McKee, J. L. McKenney, A. R. Miles, J. A. Mills, M. D. Mitchell, N. W. Moore, C. E. Myers, T. Nagayama, G. Natoni, A. C. Owen, S. Patel, K. J. Peterson, T. D. Pointon, J. L. Porter, A. J. Porwitzky, S. Radovich, K. S. Raman, P. K. Rambo, W. D. Reinhart, G. K. Robertson, G. A. Rochau, S. Root, D. V. Rose, D. C. Rovang, C. L. Ruiz, D. E. Ruiz, D. Sandoval, M. E. Savage, M. E. Sceiford, M. A. Schaeuble, P. F. Schmit, M. S. Schollmeier, J. Schwarz, C. T. Seagle, A. B. Sefkow, D. B. Seidel, G. A. Shipley, J. Shores, L. Shulenburger, S. C. Simpson, S. A. Slutz, I. C. Smith, C. S. Speas, P. E. Specht, M. J. Speir, D. C. Spencer, P. T. Springer, A. M. Steiner, B. S. Stoltzfus, W. A. Stygar, J. Ward Thornhill, J. A. Torres, J. P. Townsend, C. Tyler, R. A. Vesey, P. E. Wakeland, T. J. Webb, E. A. Weinbrecht, M. R. Weis, D. R. Welch, J. L. Wise, M. Wu, D. A. Yager-Elorriaga, A. Yu, and E. P. Yu. Review of pulsed power-driven high energy density physics research on Z at sandia. *Phys. Plasmas*, 27:070501, 2020.

[16] T. Ao, D. V. Morgan, B. S. Stoltzfus, K. N. Austin, J. Usher, E. Breden, L. M. Pacheco, S. Dean, J. L. Brown, S. Duwal, H. Fan, P. Kalita, M. D. Knudson, M. A. Rodriguez, and J. M. D. Lane. A compact X-ray diffraction system for dynamic compression experiments on pulsed-power generators. *Rev. Sci. Instrum.*, 93:053909, 2022.

[17] Tommy Ao, Kevin Austin, Eric Breden, Justin Brown, Steven Dean, Sakun Duwal, Hongyou Fan, Patricia Kalita, Marcus Knudson, Lingyao Meng, Dane Morgan, Lena Pacheco, Yang Qin, Brian Stoltzfus, Bryce Thurston, Joshua Usher, and J. Matthew D. Lane. LDRD Project 213088 Final Report: A platform-independent X-ray diffraction diagnostic for phase transition kinetics in traditional and synthetic microstructure materials. Technical Report SAND2021-12949, Sandia National Labs., 2021.

[18] Steve Plimpton. *J. Comput. Phys.*, 117(1):1–19, 1995.

[19] Charles Kittel, Paul McEuen, and Paul McEuen. *Introduction to solid state physics*, volume 8. Wiley New York, 1996.

[20] P Debye and P Scherrer. Interference on inordinate orientated particles in roentgen light. *PHYSIKALISCHE ZEITSCHRIFT*, 17:277–283, 1916.

[21] A. W. Hull. A new method of X-Ray crystal analysis. *Phys. Rev.*, 10:661–696, 1917.

[22] R. G. McQueen, S. P. Marsh, J. W. Taylor, J. N. Fritz, and W. J. Carter. *High-velocity impact phenomena*. Academic Press, New York, 1970.

[23] R. J. Trainor, J. W. Shaner, J. M. Auerbach, and N. C. Holmes. Ultrahigh-pressure laser-driven shock-wave experiments in aluminum. *Phys. Rev. Lett.*, 42:1154–1157, 1979.

[24] A. C. Mitchell and W. J. Nellis. Shock compression of aluminum, copper, and tantalum. *J. Appl. Phys.*, 52:3363–3374, 1981.

[25] L. M. Barker and R. E. Hollenbach. Shock-wave studies of pmma, fused silica, and sapphire. *J. Appl. Phys.*, 41:4208–4226, 1970.

[26] Jeffrey H. Nguyen, Daniel Orlikowski, Frederick H. Streitz, John A. Moriarty, and Neil C. Holmes. High-pressure tailored compression: Controlled thermodynamic paths. *J. Appl. Phys.*, 100:023508, 2006.

[27] Raymond F. Smith, Jon H. Eggert, Alan Jankowski, Peter M. Celliers, M. John Edwards, Yogendra M. Gupta, James R. Asay, and Gilbert W. Collins. Stiff response of aluminum under ultrafast shockless compression to 110 gpa. *Phys. Rev. Lett.*, 98:065701, 2007.

[28] James R. Asay. Isentropic compression experiments on the Z accelerator. *AIP Conf. Proc.*, 505:261–266, 2000.

[29] Clint A. Hall. Isentropic compression experiments on the sandia Z accelerator. *Phys. Plasmas*, 7:2069–2075, 2000.

[30] Dane V. Morgan, Don Macy, and Gerald Stevens. Real-time X-ray diffraction measurements of shocked polycrystalline tin and aluminum. *Rev. Sci. Instrum.*, 79:113904, 2008.

[31] Dane V. Morgan, Mike Grover, Don Macy, Mike Madlener, Gerald Stevens, and William D. Turley. Observations of shock-loaded tin and zirconium surfaces with single-pulse X-ray diffraction. *Powder Diffraction*, 25:138–142, 2010.

[32] J. W. Christian. *The theory of transformations in metals and alloys*. Pergamon, Oxford, 1965.

[33] Z. P. Tang and Y. M. Gupta. Phase transition in cadmium sulfide single crystals shocked along the c axis. *J. Appl. Phys.*, 81(11):7203–7212, 1997.

[34] S. M. Sharma and Y. M. Gupta. Wurtzite-to-rocksalt structural transformation in cadmium sulphide shocked along the a-axis. *J. Appl. Phys.*, 1998.

[35] M.D. Knudson and Y.M. Gupta. Real-time observation of a metastable state during the phase transition in shocked cadmium sulfide. *Phys. Rev. Lett.*, 81(14):2938, 1998.

[36] M.D. Knudson, Y.M. Gupta, and A.B. Kunz. Transformation mechanism for the pressure-induced phase transition in shocked cds. *Phys. Rev. B*, 59(18):11704, 1999.

[37] M.D. Knudson and Y.M. Gupta. Transformation kinetics for the shock wave induced phase transition in cadmium sulfide crystals. *J. Appl. Phys.*, 91(12):9561–9571, 2002.

[38] Nathan J Szymanski, Christopher J Bartel, Yan Zeng, Qingsong Tu, and Gerbrand Ceder. Probabilistic deep learning approach to automate the interpretation of multi-phase diffraction spectra. *Chemistry of Materials*, 33(11):4204–4215, 2021.

[39] Pedro Baptista de Castro, Kensei Terashima, Miren Garbine Esparza Echevarria, Hiroyuki Takeya, and Yoshihiko Takano. XERUS: An open-source tool for quick XRD phase identification and refinement automation. *Advanced Theory and Simulations*, 5(5):2100588, 2022.

[40] D Francom, David J Walters, John L Barber, Darby Jon Luscher, E Lawrence, Ayan Biswas, Christopher Michael Biwer, Divya Banesh, John Lazarz, Sven C Vogel, et al. Simulation and emulation of X-ray diffraction from dynamic compression experiments. *Journal of Dynamic Behavior of Materials*, 7:170–187, 2021.

[41] Yann Lecun, Yoshua Bengio, and Geoffrey Hinton. Deep learning. *Nature*, 521:436–444, 2015.

[42] Ian Goodfellow, Yoshua Bengio, Aaron Courville, and Yoshua Bengio. *Deep learning*, volume 1. MIT press Cambridge, 2016.

[43] Vijay Badrinarayanan, Alex Kendall, and Roberto Cipolla. Segnet: A deep convolutional encoder-decoder architecture for image segmentation. *IEEE transactions on pattern analysis and machine intelligence*, 39(12):2481–2495, 2017.

[44] Chaoben Du and Shesheng Gao. Image segmentation-based multi-focus image fusion through multi-scale convolutional neural network. *IEEE access*, 5:15750–15761, 2017.

[45] Zijiang Yang, Yuksel C. Yabansu, Dipendra Jha, Wei keng Liao, Alok N. Choudhary, Surya R. Kalidindi, and Ankit Agrawal. Establishing structure-property localization linkages for elastic deformation of three-dimensional high contrast composites using deep learning approaches. *Acta Materialia*, 166:335 – 345, 2019.

[46] George E Dahl, Tara N Sainath, and Geoffrey E Hinton. Improving deep neural networks for lvcsr using rectified linear units and dropout. In *2013 IEEE international conference on acoustics, speech and signal processing*, pages 8609–8613. IEEE, 2013.

[47] Dan Ciregan, Ueli Meier, and Jürgen Schmidhuber. Multi-column deep neural networks for image classification. In *2012 IEEE conference on computer vision and pattern recognition*, pages 3642–3649. IEEE, 2012.

[48] Feng Ning, D. Delhomme, Y. LeCun, F. Piano, L. Bottou, and P. E. Barbano. Toward automatic phenotyping of developing embryos from videos. *IEEE Transactions on Image Processing*, 14(9):1360–1371, 2005.

[49] Raia Hadsell, Pierre Sermanet, Jan Ben, Ayse Erkan, Marco Scoffier, Koray Kavukcuoglu, Urs Muller, and Yann LeCun. Learning long-range vision for autonomous off-road driving. *Journal of Field Robotics*, 26:120–144, 2009.

[50] Ronan Collobert, Jason Weston, Léon Bottou, Michael Karlen, Koray Kavukcuoglu, and Pavel Kuksa. Natural language processing (almost) from scratch. *J. Mach. Learning Research*, 12(ARTICLE):2493–2537, 2011.

[51] Léon Bottou. Large-scale machine learning with stochastic gradient descent. In *Proceedings of COMPSTAT'2010*, pages 177–186. Springer, 2010.

[52] Karen Simonyan and Andrew Zisserman. Very deep convolutional networks for large-scale image recognition. *arXiv preprint arXiv:1409.1556*, 2014.

[53] Kaiming He, Xiangyu Zhang, Shaoqing Ren, and Jian Sun. Deep residual learning for image recognition. In *Proceedings of the IEEE conference on computer vision and pattern recognition*, pages 770–778, 2016.

[54] Diederik P Kingma and Jimmy Ba. Adam: A method for stochastic optimization. *arXiv preprint arXiv:1412.6980*, 2014.

[55] Olga Russakovsky, Jia Deng, Hao Su, Jonathan Krause, Sanjeev Satheesh, Sean Ma, Zhiheng Huang, Andrej Karpathy, Aditya Khosla, Michael Bernstein, et al. Imagenet large scale visual recognition challenge. *International journal of computer vision*, 115(3):211–252, 2015.

[56] Olaf Ronneberger, Philipp Fischer, and Thomas Brox. U-net: Convolutional networks for biomedical image segmentation. In *International Conference on Medical image computing and computer-assisted intervention*, pages 234–241. Springer, 2015.

[57] Scott A. Roberts, Sylvain Bernard, Lincoln N. Collins, Brendan Donohoe, Collin Foster, Tyler Ganter, Benjamin Greene, Bernadette Hernandez-Sanchez, Jessica Jones, Michael C. Krygier, Tyler LaBonte, Carianne Martinez, Kyle Neal, David R. Noble, Chance Norris, Kevin Potter, Christine C. Roberts, Benjamin B. Schroeder, Krish Sharma, Matthew Smith,

and Bradley L. Trembacki. Credible, automated meshing of images. Technical Report SAND2021-11296, Sandia National Laboratories, 2021.

[58] Yarin Gal and Zoubin Ghahramani. Dropout as a bayesian approximation: Representing model uncertainty in deep learning. In Maria Florina Balcan and Kilian Q. Weinberger, editors, *Proceedings of The 33rd International Conference on Machine Learning*, volume 48 of *Proceedings of Machine Learning Research*, pages 1050–1059, New York, New York, USA, 20–22 Jun 2016. PMLR.

[59] Stefan Van der Walt, Johannes L Schönberger, Juan Nunez-Iglesias, François Boulogne, Joshua D Warner, Neil Yager, Emmanuelle Gouillart, and Tony Yu. scikit-image: image processing in python. *PeerJ*, 2:e453, 2014.

DISTRIBUTION

Hardcopy—External

Number of Copies	Name(s)	Company Name and Company Mailing Address

Hardcopy—Internal

Number of Copies	Name	Org.	Mailstop

Email—Internal (encrypt for OUO)

Name	Org.	Sandia Email Address
Technical Library	1911	sanddocs@sandia.gov

Sandia National Laboratories

Sandia National Laboratories is a multimission laboratory managed and operated by National Technology & Engineering Solutions of Sandia LLC, a wholly owned subsidiary of Honeywell International Inc., for the U.S. Department of Energy's National Nuclear Security Administration under contract DE-NA0003525.